UNIVERSITY OF CALIFORNIA
Los Angeles

Fractal Antennas: Design, Characterization, and Applications

A thesis submitted in partial satisfaction
of the requirements for the degree
Master of Science in Electrical Engineering

by

John Gianvittorio

2000

The thesis of John Gianvittorio is approved.

Elliott Brown

Tatsuo Itoh

Yahya Rahmat-Samii, Committee Chair

University of California, Los Angeles

2000

To my mother

for pushing me early on

and to my father

for telling me to never stop learning . . .

Table of Contents

1 Introduction **1**
- 1.1 Outline of Work 5

2 Survey of Literature **9**
- 2.1 Fractals 9
- 2.2 Sierpinski Sieve 10
- 2.3 Fractal Loop 12
- 2.4 Koch Dipole 12
- 2.5 Fractal Trees 13
- 2.6 Fractal Arrays 14

3 Simulation Methods **15**
- 3.1 Moment Method 15
  - 3.1.1 Moment Method Solution for EFIE 15
  - 3.1.2 Moment Method Solution for Thin Wire Radiators 17
  - 3.1.3 Surface and Wire Basis Functions 18
  - 3.1.4 Source Modeling 18
  - 3.1.5 Far Field Calculations 20

4 Fabrication Methods **22**
- 4.1 Design 22
- 4.2 Materials 25

4.3 Process 25

4.4 Testing 25

5 Fractal Loop Antennas 28

5.1 Small Loops 29

5.1.1 Fractal Generation 29

5.1.2 Antenna Analysis 31

5.1.3 Results 34

5.2 Resonant Loops 38

5.2.1 Fractal Generation 38

5.2.2 Antenna Analysis 39

5.2.3 Design Curves 40

5.2.4 Results 42

6 Fractal Dipole Antennas 48

6.1 Koch Monopole 48

6.1.1 Fractal Generation 49

6.1.2 Antenna Analysis 50

6.1.3 Antenna Characteristics 51

6.1.4 Iteration Scaling 52

6.2 Fractal Tree 54

6.2.1 Fractal Generation 55

6.2.2 Antenna Analysis 56

6.2.3 Antenna Characteristics 57

- 6.3 Three Dimensional Fractal Tree 60
  - 6.3.1 Fractal Generation 60
  - 6.3.2 Antenna Analysis 62
  - 6.3.3 Antenna Characteristics 63
- 6.4 Fractal Dipole Comparisons 64

7 Multiband Fractal Antennas 68

- 7.1 Fractal Generator and Geometry 69
- 7.2 Antenna Analysis 70
- 7.3 Antenna Characteristics 72
- 7.4 Surface Currents 76

8 Applications of Fractal Antennas 78

- 8.1 Fractal Elements in Array Antennas 79
  - 8.1.1 Reduced Mutual Coupling 79
  - 8.1.2 Tighter Array Packing 83

9 Conclusion 86

References 89

List of Figures

1.1 *Fractal Landscape 280294* by Roger B.J. Baron [1]. This landscape scene was created using a fractal. Clouds, coastlines, trees, and even water surfaces can be modeled with fractals. 2

1.2 A fly flying towards a piece of paper from very far away reveals the conundrum of defining dimensions. 2

1.3 Measuring the length of the coastline of North America exemplifies fractal geometry found in nature. 3

1.4 A fern is a common example of a geometry in nature that is easily modeled using fractal geometry. 4

1.5 The various fractal geometries that are studied in this thesis. They fall into three main categories: fractal dipoles, fractal loops, and multiband fractal dipoles. Also, applications utilizing these geometries have been studied. 7

3.1 Two variations of voltage sources as feeding models. a) Delta gap voltage generator and b) Frill voltage source. 19

4.1 Printed half loop antenna mounted over ground plane. Actual antenna and image is equivalent to loop in free space. 23

4.2 Microstrip to co-planar strip feed for printed loop antennas. . . . 24

4.3 Photograph inside anechoic chamber at the Antenna Lab at UCLA. 26

4.4 Photograph inside anechoic chamber zoomed in on fractal loop antenna on rotating pedestal. 27

5.1 Feeding configuration for two variations of a fractal loop, a Koch fractal loop and a Minkowski fractal loop. 29

5.2 Sequence for generating a Koch loop. Each iteration is generated by replacing each segment of the previous iteration with the generator. 30

5.3 Relative sizes of the loop geometries. Volume occupied by both geometries is identical. The input source is shown at the bottom of the loops. 32

5.4 Simulated real part of the input impedance for the loop antennas. 35

5.5 Simulated far field patterns for loop antennas lying in xy plane. a) xz and yz cuts b) xy cut. 36

5.6 Sequence for generating a Minkowski loop. Each iteration is generated by replacing each segment of the previous iteration with the generator. 38

5.7 Scaling factor to make a square loop that is $\lambda/4$ per side resonant for different indentation width values for a Minkowski fractal loop. 41

5.8 Relative sizes of the loop geometries for the first two iterations with an indentation width of 0.8. Each loop shown is resonant at the same frequency. 42

5.9 Far field pattern for resonant fractal loop antennas for various indentation widths and fractal iterations as computed by the moment method. The pattern cut is orthogonal to the plane of the loop. 43

5.10 Fabricated loop antennas. The loop antenna was mounted over a ground plane. Both antennas are resonant at the same frequency. 45

5.11 Fabricated loop antennas using a microstrip to co-planar strip transition. Both antennas are resonant at the same frequency. 46

5.12 Input match for fabricated loop antennas. The shift in resonant frequency is from the dielectric backing. 46

5.13 Measured far field pattern for the loop antennas at resonance. The patterns are calibrated for an accurate gain measurement. 47

6.1 Geometry of a Koch curve used as a dipole antenna. 49

6.2 First iterative steps for generating a Koch curve. 50

6.3 Simulated input match of the straight dipole and the first five iteration for the Koch dipole antennas matched to 50 Ω. 51

6.4 Simulated input impedance for the first five fractal iterations of Koch dipoles plus a straight dipole for comparison. a) Input resistance b) Input reactance 52

6.5 Far field directivity pattern for Koch dipoles of different fractal iterations. a) versus θ for $\phi = 0^o$ and $\phi = 90^o$, b) versus ϕ for $\theta = 90^o$ 53

6.6 Relative heights of a resonant Koch dipole for different fractal iterations. Only half of the dipole is shown in the figure. 53

6.7 Geometry for the feeding of a fractal tree as a dipole. 55

6.8 Geometry for the feeding of a fractal tree as a dipole. 55

6.9 Simulated input impedance matched to 50 Ω for the first five iterations of a fractal tree dipole with a split angle of 60^o and for a straight dipole. 57

6.10 Simulated input impedance for the first five iterations of a fractal tree dipole with a split angle of 60^o and a straight dipole. a) Input resistance, b) Input reactance 58

6.11 Far field pattern of a typical fractal tree antenna. This one is for a fourth iteration fractal tree with a 60^o branch split. a) E-Plane cut that is parallel to plane of branches, b) E-Plane cut that is perpendicular to plane of branches 59

6.12 A three dimensional fractal tree fed as a dipole. 60

6.13 The generation of a three dimensional fractal tree. At each iteration the branches split into four segments in two orthogonal planes. 61

6.14 A dipole and the first five iterations of a fractal tree in a dipole configuration simulated using the moment method. 62

6.15 Input match for various iterations of a three dimensional fractal tree matched to 50 Ω. 63

6.16 The simulated directivity patterns for the various iterations of the three dimensional fractal tree dipole. The pattern is taken in the $\phi = 0^o$ cut in the plane of the z directed dipole at resonance. . . . 64

6.17 Three various fractal geometries are configured as dipoles, including a Koch fractal, a fractal tree, and a three dimensional fractal tree. The starting size of each of the geometries are identical PCS band dipoles. 65

6.18 The resonant frequency for each of the fractal antennas versus the number of iterations for a Koch fractal, a fractal tree, and a three dimensional fractal tree in a dipole configuration as simulated with the moment method. 66

6.19 Simulated input resistance versus the number of generating iterations for three fractal antennas. 67

7.1 Sierpinski sieve fractal fed as a dipole. 69

7.2 Generation of a Sierpinski sieve, starting with a bowtie antenna. . 70

7.3 Relative sizes of antennas used for multiband comparison. 70

7.4 Triangular facets and feed wire for Sierpinski antenna simulations. 71

7.5 Simulated input match of antennas matched to 50 Ω. 72

7.6 Input match of antennas matched to 50 Ω plotted on a logarithmic scale. 73

7.7 Simulated far field pattern of antennas at first resonance. a) $\phi = 0^o$ cut b) $\phi = 90^o$ cut. 74

7.8 Simulated far field pattern of antennas at second resonance. a) $\phi = 0^o$ cut b) $\phi = 90^o$ cut. 75

7.9 Simulated far field pattern of antennas at third resonance. a) $\phi = 0^o$ cut b) $\phi = 90^o$ cut. 75

7.10 Currents on Sierpinski 3 dipole at a) first resonance, 5 GHz, b) second resonance, 11 GHz, c) third resonance, 24 GHz 76

7.11 Currents on bow 3 dipole at a) first resonance, 5 GHz, b) second resonance, 11 GHz, c) third resonance, 24 GHz 77

8.1 Array of two fractal square loops. Separation distance is the shown as the distance between the edges of the elements. 79

8.2 a) Far field patterns and b) S11 input impedance matched to 50 Ω for the loop elements used in the arrays of this chapter. The relative sizes of the two loops is drawn inset in (a). 80

8.3 Relative geometry for the two arrays using a) Minkowski square loop elements, and b) using standard square loop elements. The space between the elements is increased for the array with fractal elements. 81

8.4 Normalized, simulated directivity patterns for 5 element, Dolph-Chebyshev, 0.3λ spaced linear array scanned to 150^o. The three plots shown include the simulated patterns using fractal square elements, square elements, and the ideal pattern as expected without mutual coupling. 82

8.5 Simulated received power by the end element of the array with the other 4 elements radiating normally. 83

8.6 Relative geometry for the two arrays using a) Minkowski square loop elements, and b) using standard square loop elements. The total width of the array is maintained for the two arrays. The edge-to-edge separation between the elements is similar for the two arrays. 85

8.7 Simulated directivity patterns for a 5 element, 0.5λ spaced array of square elements and a 7 element, 0.35λ spaced array of fractal elements, both scanned to 150^o, uniformly excited, and having equal total lengths. Also plotted are the ideal patterns of the 5 and 7 element arrays with uniform excitation neglecting mutual coupling. 85

List of Tables

2.1 Relevant references for fractal antennas sorted by category. 10

4.1 Electrical properties of substrates used of for fabrication 25

5.1 Directivity data for the loop antennas over varying indentation widths and fractal iterations. All of the antennas are resonant at the same frequency. 44

6.1 Height and length of Koch fractal antennas in terms of wavelengths at resonance. 54

6.2 Length of each straight section of the fractal tree for the first five iterations. 56

6.3 Length of each segment of the three dimensional fractal tree for the first five iterations. 61

8.1 Specifications used in the design of arrays showing reduced mutual coupling with fractal elements. 81

8.2 Specifications used in the design of arrays showing denser packing with fractal elements. 84

ACKNOWLEDGMENTS

I would like to thank my advisor, Professor Yahya Rahmat-Samii, for his ideas, support and guidance throughout this work. I would also like to thank Professors Tatsuo Itoh and Elliott Brown for serving on my masters thesis committee.

I also thank my colleagues in Professor Yahya Rahmat-Samii's research group at UCLA, for their advice and discussions.

Special thanks is also given to my parents and family for their support and encouragement through all of my pursuits over the years.

Also, this work was supported in part by the US Army Research Office under contract DAAH04-96-1-0389.

Abstract of the Thesis

Fractal Antennas: Design, Characterization, and Applications

by

John Gianvittorio

Master of Science in Electrical Engineering
University of California, Los Angeles, 2000
Professor Yahya Rahmat-Samii, Chair

'Fractals' were first defined by Benoit Mandelbrot in 1975 as a way of classifying structures whose dimensions were not whole numbers. These geometries have been used previously to characterize unique occurrences in nature that were difficult to define with Euclidean geometries, including the length of coastlines, the density of clouds, and the branching of trees.

Antenna design can benefit from studying these geometries. Looking at geometries whose dimensions are not limited to integers may lead to the discovery of antennas with improved characteristics over that which exist today. Fractal antennas have shown the possibility to miniaturize antennas and to improve input matching. Certain classes of fractal antennas can be configured to operate effectively at various frequency bands.

There are three distinct advantages which are studied in this thesis by using fractal antennas. First, fractal geometries can be implemented to miniaturize resonant loop and dipole antennas. Also, designing with fractal geometries can overcome limitations to improve the input resistance of antennas that are typically

hard to match to feeding transmission lines. Furthermore, the self-similar nature in the fractal geometry can be utilized for operating a fractal antenna at various frequencies.

Fractal antennas can be utilized in a variety of applications, especially where space is limited. An example of exploiting the benefits of fractals in antenna systems are phased arrays, where fractals can reduce mutual coupling and allow for lower scan angles.

CHAPTER 1

Introduction

Fractal geometries have found an intricate place in science as a representation of some of the unique geometrical features occurring in nature. Fractals are used to describe the branching of tree leaves and plants, the sparse filling of water vapor that forms clouds, the random erosion that carves mountain faces, the jaggedness of coastlines and bark, and many more examples in nature.

The complexity of the situation can be surmised in the following visualization, depicted in Figure 1.2, of a microscopic fly flying towards a piece of paper [2]. The fly starts out very far from the object, in Figure 1.2 (a), thus it appears as a zero-dimensional speck. As the fly gets closer, in Figure 1.2 (b), the speck begins to elongate into a one-dimensional line. Upon flying over the line, in Figure 1.2 (c), the fly sees that it is actually a two-dimensional plane. Flying even closer in Figure 1.2 (d), the fly sees that the plane has a depth to it, as well, forming a three-dimensional prism; followed by flying closer still, sees only a two-dimensional plane. Finally, the fly flies into the piece of paper, seeing a one-dimensional network of fibers.

Another classical conundrum depicting the need for fractal geometry is the attempt to measure a coastline, like the coastline of North America shown in Figure 1.3. As an example in this thought experiment, say a surveyor were to use a ruler that is 1 kilometer long to measure the length by counting the number of rulers, lined up end to end, that fit around the coast. By multiplying the

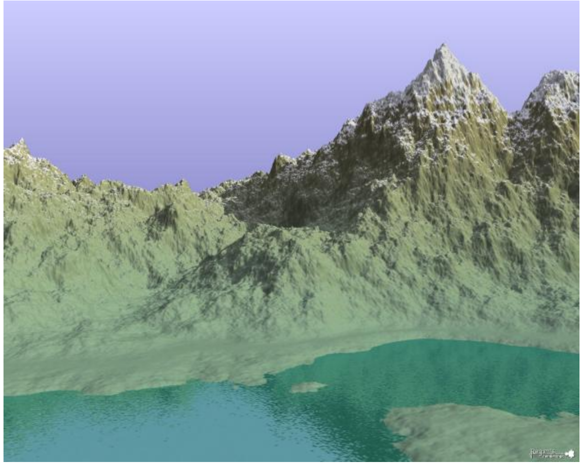

Figure 1.1: *Fractal Landscape 280294* by Roger B.J. Baron [1]. This landscape scene was created using a fractal. Clouds, coastlines, trees, and even water surfaces can be modeled with fractals.

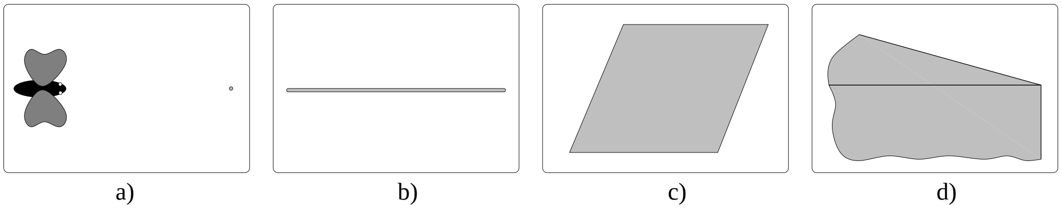

Figure 1.2: A fly flying towards a piece of paper from very far away reveals the conundrum of defining dimensions.

Figure 1.3: Measuring the length of the coastline of North America exemplifies fractal geometry found in nature.

number of rulers by 1 kilometer, he has an approximate measure of the length of the coast. However, if he switches to a ruler that is only 1 meter in length and repeats the experiment, the result will be different. The 1 meter ruler will measure inside coves and lagoons that the 1 kilometer ruler smoothed over. Likewise, a 1 centimeter ruler will measure around rocks that the 1 meter ruler missed. This can continue down to the atomic scale, with the measured length of the coast increasing every time. While the coast of North America fits in a finite volume on earth, it is possible to take this thought experiment to the limit and suggest that with a ruler small enough, the surveyor will measure the length to be infinite! This is a Zeno paradox that was studied by ancient Greeks [3].

Therefore, there is a need for a geometry that handles these complex situations better than Euclidean geometry. Euclidean structures have whole number dimensions, such as a one dimensional line or a two dimensional plane. Benoit Mandelbrot first defined the term 'fractal', meaning fractional dimension, in 1975 to handle geometries with dimensions that do not fall neatly into a whole number category. One property of a certain class of fractals, as seen in the previous

Figure 1.4: A fern is a common example of a geometry in nature that is easily modeled using fractal geometry.

coastline example, is the unique property that it can have an infinite length while fitting in a finite volume.

Fractals, as used in this work, are structures of infinite complexity with a self-similar nature. What this means, is that as the structure is zoomed in upon, the structure repeats. There never is a point where the fundamental building blocks are found. This is because the building blocks themselves have the same form as the original object with infinite complexity in each one.

An example of this in nature can be seen in a fern, shown in Figure 1.4. The entire frond has the same structure as each branch. If the individual branches were zoomed in upon, it is quite conceivable to imagine this as a completely separate frond with branches of its own.

The idea of a dimension that is in between those of Euclidean geometries has opened up a new range for many applications, one of which being electromagnetic systems. It can be used to develop new configurations for radiators and reflectors. It might be possible to discover antennas that give us better performance than any Euclidean geometry could provide.

1.1 Outline of Work

In this thesis, various fractal geometries are investigated as antennas. There are an infinite number of possible geometries that are available to try. The ones tried here provide a broad overview of several different classes and their various characteristics. The fractals that are investigated are all deterministic and truncated.

Deterministic fractals have a predefined geometry. Fractals can have a random component in them that allows for better modeling of the randomness of nature. If the fern from the previous section is observed, the branches of the individual frond have varying lengths. The fractal that is used to generate a mathematical model could also, therefore, allow the branches to be of various lengths. All of the fractals that are studied here do not have this random quality. There is a predefined and repeatable generating methodology for each of the geometries.

Another key aspect of using fractals as antennas is the need to truncate the generating procedure. While an ideal fractal may have an infinite complexity like the ever increasing length of a coastline, the infinitesimally small details do not affect the performance of a radiator. The point of truncation is not something that can be discussed here globally for all of the fractals that are studied. Rather, in the individual sections this area is covered for each of the particular geometries. In this thesis, the performance of antennas generated with various numbers of iterations are observed. By comparing the performance of a series of truncated fractals, trends emerge which allude to the ideal performance of a fractal that may not be directly observable due to fabrication or simulation limitations. The concept of generating fractals by iterations is best conveyed with examples and is shown in the beginning of each section for the relevant geometry.

Fractals as antennas are simulated using the moment method. The basics of the simulation method and the code that is used are discussed in chapter 3. In addition, several of the antennas are fabricated. These methods are discussed in chapter 4.

The classes of fractals that are studied are outlined in Figure 1.5. The three cases are fractal dipoles, fractal loops, and fractal multiband antennas. In addition, applications that utilize fractal antennas are investigated.

Fractal dipoles are wire antennas. The fractal structure is mirrored on either side of the generator. These antennas are mostly compared to straight dipoles at resonance. One can expect that using a fractal over a straight Euclidean dipole can miniaturize the antenna, while maintaining performance. The structures that are studied include a Koch fractal, a fractal tree structure and a three dimensional version of the fractal tree. The geometries of each of these are explained in detail in chapter 6.

Fractal loop antennas are closed island fractals that are fed as loop antennas. These are compared with Euclidean circular and square loop antennas at resonance and below resonance. The expectation for this type of antenna is that the size is miniaturized for resonant antennas, while the input resistance is improved for fractal antennas configured for operation below resonance. The geometries of each of these are explained in chapter 5.

While all fractals are inherently multiband due to the scaled self-similarity in their structures, another section explores one type of fractal that is particularly suited for multiband operation, a Sierpinski sieve. The characteristics at each resonance are compared and some physical explanations on the nature of why it operates so well as a multiband antenna are given in chapter 7.

Finally, the antennas are applied to some unique applications and are sim-

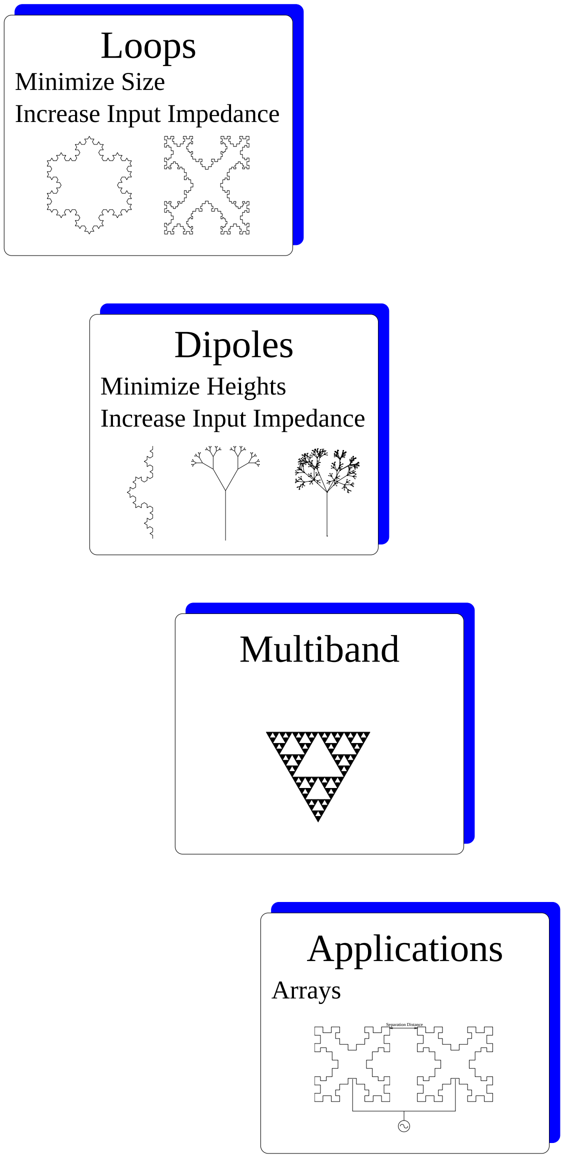

Figure 1.5: The various fractal geometries that are studied in this thesis. They fall into three main categories: fractal dipoles, fractal loops, and multiband fractal dipoles. Also, applications utilizing these geometries have been studied.

ulated in such configurations. In chapter 8, applications for these particular antennas are proposed and developed. These examples include applications requiring miniaturized antennas. One of these applications that is investigated and developed is fractal elements in arrays. The miniaturized elements reduce mutual coupling between the elements allowing for more robust and reliable designs. It also allows tighter packing of elements, lowering the allowable scan angles for arrays.

CHAPTER 2

Survey of Literature

There has been a lot of interest in fractal antennas recently. Since Mandelbrot first defined the geometry, fractals have found many applications. Their use as antennas is one of these unique applications. Presented below is a summary of the publications resulting from some of the research on fractal antennas.

A quick reference table to locate references is provided in Table 2.1.

2.1 Fractals

Fractal geometry was first defined by Benoit Mandelbrot [39, 2], to define many perplexing geometries found in nature.

A good reference on the basics of fractal geometry, especially on how they pertain to the field of electrodynamics can be found in [4]. It provides a tutorial on fractal geometry, outlining the necessary vocabulary of the field.

Specific to antennas, an interesting analysis of some classical frequency-independent antennas using fractal geometric principles is investigated in [5] and [6].

Reference [7] serves as an overview article of many of the possibilities of using fractals. The authors present some fractal geometries as fractal elements as well as arrays.

The book [8] includes a compilation of papers on fractals applied to electro-

Table 2.1: Relevant references for fractal antennas sorted by category.

Fractals		
		[2] [4] [5] [6] [7] [8] [9]
Fractal Elements		
	Sierpinski Sieve	
		[10] [11] [12] [13] [14] [15]
		[16] [17] [18] [19] [20] [21]
	Fractal Loop	
		[22] [23] [24]
	Koch Dipole	
		[25] [26] [14]
	Fractal Trees	
		[27] [28] [17] [29]
Applications		
	Fractal Arrays	
		[30] [31] [32] [33] [34] [35]
		[36] [37] [38]

magnetics.

A recent publication that serves as a very good reference for fractal antennas as elements and as arrays is [9].

2.2 Sierpinski Sieve

This multiband antenna, which is explored in chapter 7, has been exhaustively researched previously. Carlos Puente has published four works of interest on this antenna. A thorough description and experimentation is documented in [10] and [11]. The authors present variations on the Sierpinski geometry and present the effects of these variations on the characteristics of the antenna in [12] and [13]. These two papers describe the effects of modifying the geometry of the Sierpinski gasket. The desired changes are improved matching and control of the multiple bands.

The Sierpinski antenna is fabricated and measured verifying previous results in [14].

The simulated predictions of the current distribution over the Sierpinski sieve antenna showing the multiband nature of the antenna were verified using infrared thermograms in [15]. The authors fabricated the antenna and measured the current distribution with a near field thermogram technique.

In [16], an efficient numerical model is presented for predicting the input performance of a Sierpinski sieve antenna. The numerical models are compared with measured input matches of fabricated Sierpinski sieve antennas.

Similar experimentation showing how the multiband characteristics of the Sierpinski sieve antenna is unique to this geometry and not all fractals is shown in [17]. In this work, the Sierpinski sieve is compared to a Sierpinski carpet, a similar geometry with a square starting shape rather than a triangle, as is the case for a Sierpinski sieve. The results do not show a multiband characteristic like that found with the Sierpinski sieve.

The Sierpinski sieve antenna was also analyzed using the time-domain electric-field integral equation using a marching-on-in-time procedure in [18].

This type of antenna has been explored in other configurations, as well. In [19], the author shows how sandwiching the antenna between scaled copies of itself increases the bandwidth of the antenna. While a single Sierpinski gasket has distinct bands, this technique can be used to improve the match between bands. Improved bandwidth using this technique and variations of the Sierpinski carpet fractal were shown in [20].

Another use of the Sierpinski gasket was explored in [21]. Here, the fractal geometry was utilized to develop a multiband frequency selective surface (FSS).

2.3 Fractal Loop

Fractal loops have been studied as a means of miniaturizing loop antennas. In [22], [23] and [24], the author describes some of the basic parameters of fractals and their relevant benefits as antennas. In these papers, a Minkowski square loop is simulated and used as a Ham radio antenna. This type of antenna is studied here in detail in chapter 5.2.

Also in [23] is the use of these closed loop fractals as sparse meshes to be used as ground planes.

2.4 Koch Dipole

The Koch Dipole has been researched as a means of miniaturizing dipole antennas. The details about their geometry and performance of this geometry as an antenna are in chapter 6.1. There have been several works which have looked into this topic. A descriptive source of information on this antenna can be found in [25]. They describe the miniaturization effects as they relate to the iteration of the fractal.

The Koch dipole is also used in [26] in an investigation of the necessary requirements for frequency independent antennas.

The Koch monopole antenna is fabricated and measured verifying previous results in [14].

2.5 Fractal Trees

Fractal antennas that have been designed to mimic the branching property of trees have been investigated in some detail, as well. They are covered here in chapter 6.2.

Electrochemical deposits that grow into tree like patterns have been studied in [27]. This particular type of fractal is not deterministic like the other fractals that have been observed. This type of fractal is grown randomly resulting in variously scaled branches. The idea of this line of research was to observe the multiband results of this fractal from the variations of scale in the geometry.

A deterministic fractal tree was studied in [28]. Here, the authors studied the correlation between the fractal dimension and the resulting input match. The tree fractal that was used is variational enough to easily control the fractal dimension.

In [17], the authors explore the multiband characteristics of a deterministic tree fractal. A correlation is made between the number of resonant bands and the fractal iteration of the geometry.

In [29], the authors study a two-dimensional ternary tree antenna as a monopole over a ground plane. The antenna shows distinct resonances corresponding to the self-similar scales in the geometry. Between the bands, however, the input resistance is very low, leading the authors to suggest that the structure could be well suited as a multiband filter or absorber.

2.6 Fractal Arrays

Fractal geometries can be applied to the design of arrays. Fractal elements used in uniformly spaced arrays has been studied in this thesis in chapter 8. Fractals are also utilized in array design to define the spacing of the elements.

The idea of using fractal spacing for arrays has been investigated by several researchers. In references [30, 31, 32], the spacing of the array was shaped using fractal geometries, while the elements were standard Euclidean shapes. Article [32] is a very thorough study on this topic.

Arrays with the distribution of a Cantor set has been the topic of these papers, [33, 34].

A Cantor set distribution is also implemented in [35, 36] for the spacing of an array. Similar features of the patterns of the arrays compare to similarities in the spacing geometry. Also, Cantor sets of different fractal dimension are simulated, showing a correlation between the maximum side lobe level and the fractal dimension.

A derivation of the radiation patterns for Cantor sets of distributed currents is presented in [37].

In paper [38], the authors present an analysis of array elements in a Sierpinski carpet configuration to create sum and difference patterns.

CHAPTER 3

Simulation Methods

Designing antennas and radiating systems requires robust simulation tools to obtain accurate characterization. The method that is utilized throughout this thesis is a moment method code developed at UCLA [40]. In the following section, an overview of the moment method process pertaining to the simulations completed in this thesis is presented [41].

3.1 Moment Method

The moment method is a numerical technique for solving an integral equation whose integrand is the current density on the body of interest. The body may either be a length of perfectly electrical conducting wire or a perfectly electrical conducting surface. In the simulations that were performed in this thesis, dielectrics are not simulated. However, in general, the moment method can be used in simulations involving metallic bodies and dielectrics.

3.1.1 Moment Method Solution for EFIE

The integral equation that is solved is the electrical field integral equation (EFIE). The equation applies to perfect electrical conductors (PEC). The currents are found by imposing the condition that tangential electric fields vanish on the surface of the conductors

$$\mathbf{E}^{total}_{tangential} = \mathbf{E}^{incident}_{tangential} + \mathbf{E}^{scattered}_{tangential} \tag{3.1.1}$$

The incident field is the field that would exist if the conducting surfaces would be absent. The scattered fields are those that are generated from the induced surface currents. The equivalence theorem can be utilized to remove the conducting bodies and define a sheet of current that will excite the true scattered field, which is excited by the induced surface currents. This field from these equivalent currents can be computed from Maxwell's equations. The solution of Maxwell's equations for an electric field at an observation point r can be found using auxiliary potential functions, the magnetic vector potential, $\mathbf{A}$, and the electric scalar potential, Φ.

$$\mathbf{E}^{scattered} = -j\omega\mathbf{A}(r) - \nabla\Phi(r) \tag{3.1.2}$$

Eq. (3.1.2) substituted into Eq. (3.1.1) results in the Electric Field Integral Equation (EFIE)

$$[-j\omega\mathbf{A}(r) - \nabla\Phi(r)]_{tangential} = -\mathbf{E}^{incident}_{tangential}(r) \tag{3.1.3}$$

where,

$$\mathbf{A}(r) = \mu\int_S \mathbf{J}(r')G(r,r')dS' \tag{3.1.4}$$

$$\Phi(r) = -\frac{1}{j\omega\epsilon}\int_S \nabla'\bullet\mathbf{J}(r')G(r,r')dS' \tag{3.1.5}$$

$$G(r, r') = \frac{e^{-jkR}}{4\pi R} \tag{3.1.6}$$

and $R = |r - r'|$ is the distance between an observation point r and the source point r' and $k = \frac{2\pi}{\lambda}$, with λ being the wavelength. S is a surface that supports a sheet of current. The sheet does not have to be continuous.

The moment method is applied to Eq. (3.1.3) to solve for the surface currents, $\mathbf{J}$. To accomplish this, it is necessary to represent the unknown currents, $\mathbf{J}$, in terms of a set of basis functions, $\mathbf{f}_n$

$$\mathbf{J}(r') = \sum_{n=1}^{N} I_n \mathbf{f}_n(r') \tag{3.1.7}$$

where I_n are the unknown current coefficients. Substituting Eq. (3.1.7) into Eq. (3.1.3) results in a set of N linear equations that provide an approximation to the true solution. The solution converges to the true solution as $N \to \infty$.

3.1.2 Moment Method Solution for Thin Wire Radiators

For wire radiators, the calculations can be simplified by using the thin wire approximation. This assumes that the wire radius, a, is much smaller than a wavelength, λ. Thus, the current density, $\mathbf{J}$ is uniformly distributed around the circumference of the wire

$$\mathbf{J} = \frac{I\hat{\mathbf{l}}'}{2\pi a} \tag{3.1.8}$$

where $\hat{\mathbf{l}}'$ is a unit vector along the axis of the wire and I is the total current passing through a cross section of the wire. This expression for the current is then substituted into the vector and scalar potential functions, Eq. (3.1.4) and Eq. (3.1.5), using the substitution $dS' = ad\phi' dl'$.

$$\mathbf{A}(r) = \frac{\mu}{4\pi} \int_{\Gamma_w} I \hat{\mathbf{l}}' K(r, r') dl' \qquad (3.1.9)$$

$$\Phi(r) = -\frac{1}{j4\pi\omega\epsilon} \int_{\Gamma_w} \frac{dI}{dl'} K(r, r') dl' \qquad (3.1.10)$$

where instead of the free space Green's function, Eq. (3.1.6), K, is used.

$$K(r, r') = \frac{1}{2\pi} \int_{-\pi}^{\pi} \frac{e^{-jkR}}{R} d\phi \qquad (3.1.11)$$

3.1.3 Surface and Wire Basis Functions

The currents on the body surfaces and wires are approximated using a generalized triangular basis function. The bodies are modeled as a set of triangular facets. For the general case,

$$\mathbf{f}_n(r') = \frac{\rho}{h_n} \qquad (3.1.12)$$

where ρ is a vector identifying the direction of the current and h is either the height of the triangular facet for bodies or the length of the segment for wires. These basis functions are defined over the metallic surfaces or wires of interest.

3.1.4 Source Modeling

The feeds for the antennas and radiating structures can be modeled using ideal voltage sources. These sources are used to calculate the incident field, $\mathbf{E}^{incident}_{tangential}$, in Eq. (3.1.1).

An ideal voltage source forces a voltage at a particular part of the structure. For the work completed here, the voltage is forced in a gap between wires. There

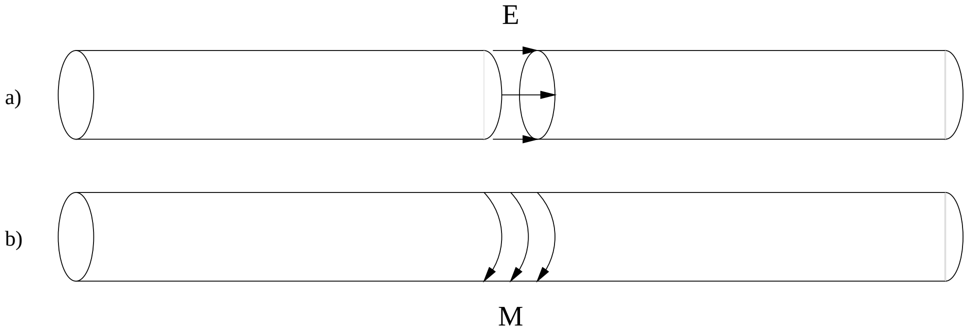

Figure 3.1: Two variations of voltage sources as feeding models. a) Delta gap voltage generator and b) Frill voltage source.

are two voltage sources of interest that are utilized in the modeling, both are depicted in Figure 3.1.

The first voltage source type is called a *delta gap* source. This source forces the voltage at one node on a wire to a fixed value. The gap is infinitesimally small, hence the requirement of a *Dirac delta* function to accurately mathematically model the voltage.

Another type of source model is called a *voltage frill* model. Instead of assuming a fixed voltage only in the gap of a wire, a voltage frill models the equivalent magnetic loop induced by a ribbon of electric field that exists around the edge of the gap of the wire. This loop induces a tapering voltage along the length of the wire, rather than only at the gap.

A benefit of using a frill source over a delta gap source is its improved modeling of coax antenna feeds, a popular way to feed fabricated antennas. The width of the magnetic loop is specified with a frill source, which directly correlates with the dimensions of the coax probe. The improved modeling leads to more accurate predictions of the input impedance.

Using these voltage sources also allows for accurate modeling of array antennas. Multiple voltage sources can be supplied, with varying excitation levels and phases. Modeling arrays in this manner is very effective because mutual coupling between all radiating elements is taken into consideration.

3.1.5 Far Field Calculations

The radiation patterns from the simulated antennas can be calculated by radiating the computed currents. This can be done using the standard far field approximations.

$$\mathbf{E} = -j\omega \mathbf{A}_T \tag{3.1.13}$$

$$\mathbf{H} = -\frac{j\omega}{\eta}\hat{\mathbf{r}} \times \mathbf{A}_T \tag{3.1.14}$$

where $\eta = \sqrt{\frac{\mu}{\epsilon}}$ and $\hat{\mathbf{r}}$ is a unit vector in the observed direction of the far field,

$$\hat{\mathbf{r}} = \hat{\mathbf{x}} \sin\theta \cos\phi + \hat{\mathbf{y}} \sin\theta \sin\phi + \hat{\mathbf{z}} \cos\theta \tag{3.1.15}$$

and $\mathbf{A}_T$ denotes the transverse component of $\mathbf{A}$, which in the far field reduces to

$$\mathbf{A}(r) = \frac{\mu}{4\pi}\frac{e^{-jkr}}{r}\int_S \mathbf{J}(\mathbf{r}')e^{-jk\hat{\mathbf{r}}\bullet\mathbf{r}'}dS' \tag{3.1.16}$$

The directivity of the antenna is calculated from

$$D(\theta, \phi) = 4\pi\frac{U(\theta, \phi)}{P_{in}} \tag{3.1.17}$$

where the radiation intensity, $U(\theta, \phi)$ (W/unit solid angle), is a far field parameter that is independent of r. It can be found from both polarization components of the scattered electric field,

$$U(\theta, \phi) = \frac{1}{2\eta}(|E_\theta(\theta, \phi)|^2 + |E_\phi(\theta, \phi)|^2) \tag{3.1.18}$$

The power supplied to the antenna is computed from the sum of the applied voltage sources and the computed currents. Therefore, for N voltage sources, the power input to the antenna would be

$$P_{in} = \sum_{i=1}^{N} \frac{1}{2} \Re(V_i I_i^*) \tag{3.1.19}$$

CHAPTER 4

Fabrication Methods

In addition to simulating the performance of the antennas, several of the final designs were fabricated and tested in the anechoic chamber at UCLA [42].

The antennas were fabricated by printing the design on a piece of copper clad dielectric. The methodology of how this was done is laid out in the next sections.

4.1 Design

The fractal antennas were designed and simulated as metallic bodies in free space, which works very well in simulation, but is difficult to fabricate. These antennas were built by printing them on a piece of dielectric. The antennas that were fabricated were designed as wire antennas. Printing them on a substrate slightly changes the dimensions of the antenna by slowing the electromagnetic waves passing through the dielectric. This causes the antenna to look electrically bigger than it really is. The equation to compensate for this is presented below.

As with dipoles, loop antennas require a balun to generate positive and negative feeds for the antenna. For dipoles, a popular feeding technique is to mount the monopole over a ground plane. The image then becomes the negative half of the antenna. The same principle was used to fabricate a loop antenna. One half of the loop antenna was printed on a piece of dielectric and mounted over a ground plane as shown in Figure 4.1. One end of the printed loop was fed with

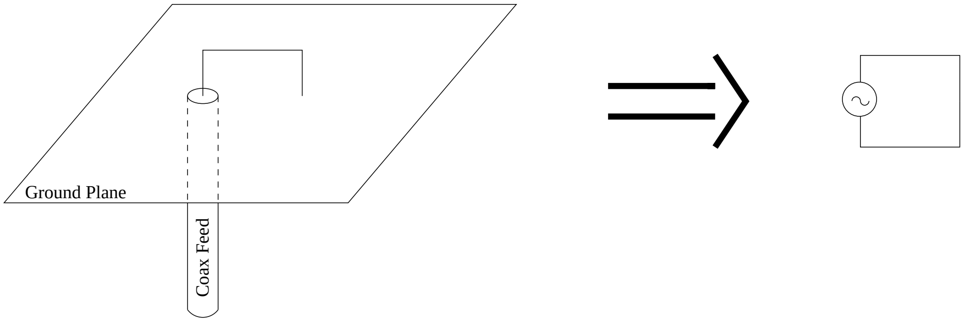

Figure 4.1: Printed half loop antenna mounted over ground plane. Actual antenna and image is equivalent to loop in free space.

a coax feed through the ground plane, as a monopole would be fed. The other end was touching the ground plane. For a resonant loop antenna the current at this end of the antenna should be zero, thus having it touch the ground plane has little effect. The ground plane is a flat piece of copper sheeting.

Using image theory, the currents can be predicted to operate in exactly the same fashion as a loop in free space.

The disadvantages of this method are that it requires a large ground plane and very careful manufacturing. Because only half of the antenna is fabricated, the depth of the coax probe through the ground plane is very critical to setting the length of the perimeter of the loop.

Another method was developed to make the antennas more precisely manufacturable. The exact dimensions of the loop could be better controlled if the entire loop could be printed instead of just half.

A co-planar strip feed was utilized as a balun. A co-planar strip includes two transmission lines that are 180^o out of phase with each other. A microstrip feed and delay line was used to feed the co-planar strip lines out of phase.

This feeding network is shown in Figure 4.2.

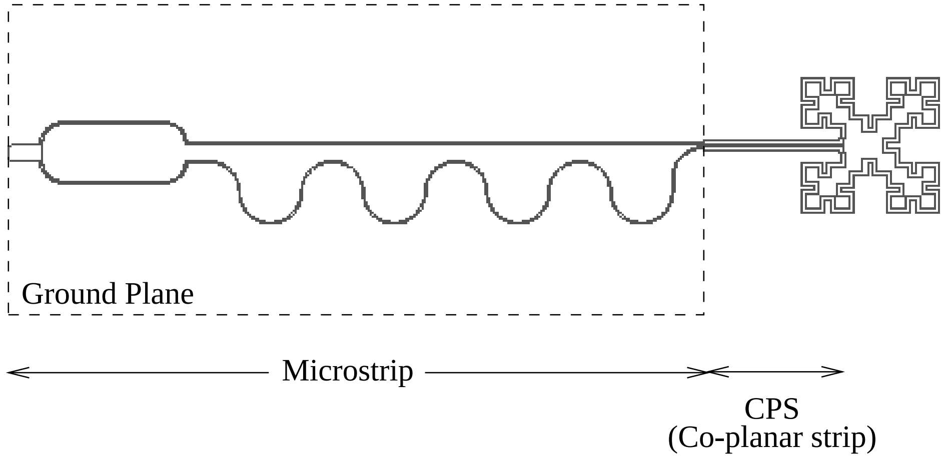

Figure 4.2: Microstrip to co-planar strip feed for printed loop antennas.

The first section includes a microstrip transmission line and splitter feeding delay lines, which in turn feeds the co-planar strip. As can be seen in the figure, the ground plane is only under the microstrip section. The co-planar strips do not require a ground plane beneath the dielectric.

Having a piece of dielectric behind any printed antenna serves to slow down the electromagnetic wave making the antenna seem electrically larger. The resulting shift in frequency is calculated by assuming the effective dielectric that is seen by the antenna is an average between the dielectric material and free space as predicted in Eq. (4.1.1)

$$\lambda_{effective} = \lambda_0 \frac{1}{\sqrt{\frac{\epsilon_{relative}+1}{2}}} \tag{4.1.1}$$

The printed antenna can also excite surface waves in the substrate depending on its thickness and dielectric constant. These waves are not simulated in this thesis. These antennas can be printed on thin, low dielectric substrates that do not support surface waves.

4.2 Materials

The antennas were printed on different Duroid material. The specifications for the different dielectrics are given in Table 4.1

Table 4.1: Electrical properties of substrates used of for fabrication

	$\epsilon_{relative}$	thickness (mils)	CU thickness (mils)	loss tangent
Rogers 5880	2.33	62	15	0.0009
Rogers 6006	6.15	50	15	0.0009
Rogers 5880	2.33	25	15	0.0009

4.3 Process

The antennas were printed using standard photolithography and etching techniques. The mask is made by transferring the antenna outline onto a piece of Ruby-Lithe, photolithography film. The copper clad substrate is cleaned and evenly coated with photoresist and baked to allow the photoresist to set. The coated substrate is then exposed to UV light in a light box using the Ruby-Lithe mask to block the areas where the metal will remain. The circuit is then etched in a FeCl solution. The complete process is outlined in [43].

4.4 Testing

The antennas were tested in an anechoic chamber in the Antenna Lab at UCLA. The measurement chamber is 9 feet x 8 feet x 18 feet 9 inches. The patterns are measured using an Orbit/FR 959 Automated Antenna Measurement Workstation controlling a HP 8510B network analyzer. The chamber is illuminated with an

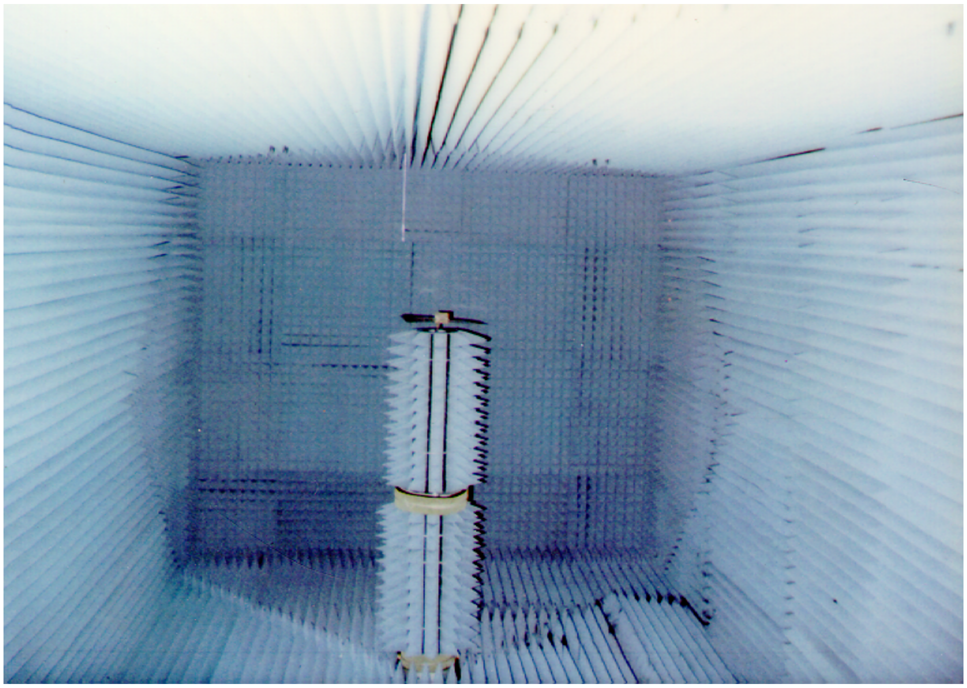

Figure 4.3: Photograph inside anechoic chamber at the Antenna Lab at UCLA.

AEL 1498 horn antenna. The operating frequency range of the chamber is 2-18 GHZ. A picture taken inside the chamber while testing a fractal loop antenna is shown in Figure 4.3. A zoomed photograph of the antenna on the rotating pedestal is shown in Figure 4.4.

Figure 4.4: Photograph inside anechoic chamber zoomed in on fractal loop antenna on rotating pedestal.

CHAPTER 5

Fractal Loop Antennas

Loop antennas are well understood and have been studied using a variety of Euclidean geometries. They have distinct limitations, however. Resonant loop antennas require a large amount of space and small loops have very low input resistance. A fractal island can be used as a loop antenna to overcome these drawbacks. Two possible fractals fed as loop antennas are depicted in Figure 5.1.

The fractals are variations of Minkowski and Koch islands. These types of fractals are commonly used to model unique geometries found in nature from snowflakes to coastlines.

Fractal loops have the characteristic that the perimeter increases to infinity while maintaining the volume occupied. This increase in length decreases the required volume occupied for the antenna at resonance. For a small loop, this increase in length improves the input resistance. By raising the input resistance, the antenna can be more easily matched to a feeding transmission line.

These antennas have been simulated using the moment method. The resonant loop antennas were fabricated and tested as described in chapter 4.

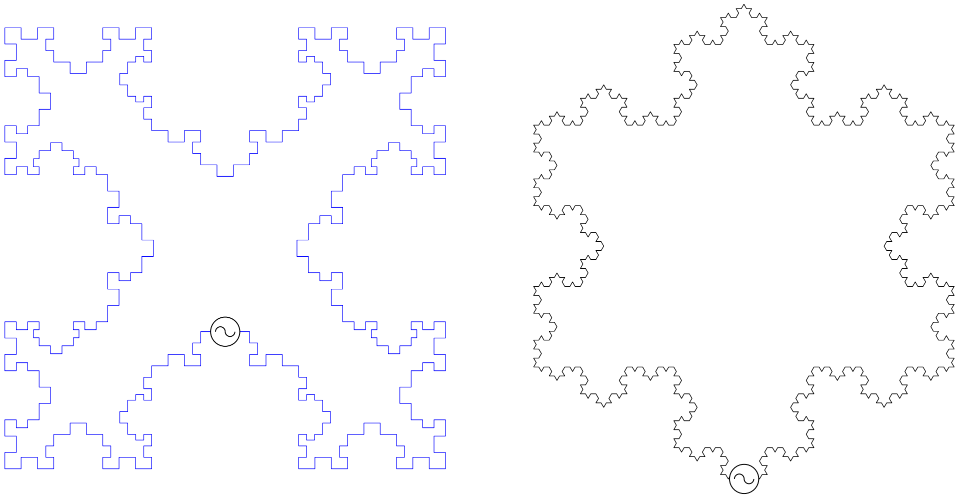

Figure 5.1: Feeding configuration for two variations of a fractal loop, a Koch fractal loop and a Minkowski fractal loop.

5.1 Small Loops

Small loop antennas are known to have a low input resistance. Therefore, matching the antenna to a 50 Ω feed line can be difficult. Fractal loops can be used to increase the input resistance of a small loop antenna. A Koch island loop that fits inside of a small circular loop can be shown to have a much higher input resistance.

5.1.1 Fractal Generation

The starting pattern for the Koch island that is used as a fractal antenna is a triangle. From this starting pattern, every segment of the starting pattern is replaced by the generator. The first four iterations are shown in Figure 5.2 to exemplify the process. One iteration of replacing a segment with the generator is shown in the bottom of Figure 5.2. The starting pattern is Euclidean and, therefore, the process of replacing the segment with the generator constitutes the

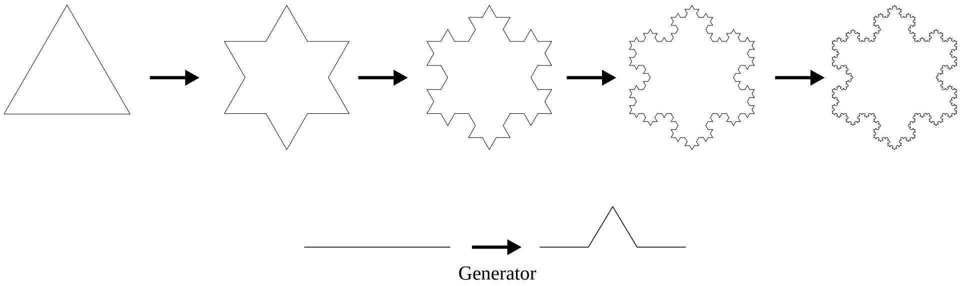

Figure 5.2: Sequence for generating a Koch loop. Each iteration is generated by replacing each segment of the previous iteration with the generator.

first iteration.

The generator is a straight segment that has been broken into three equally sized pieces. The middle section is removed and replaced with two straight pieces of the same length as the one removed. They fit into the original gap in a equilaterally triangular fashion. Therefore, the resulting shape, the generator, retains the same overall length. The total length of the generator, however, is one third longer than it was previously.

Each of the three sides of the starting triangle is replaced with the generator. This resulting shape then becomes the new starting pattern. Each segment in this new shape is then replaced with the generator. The generator is scaled at every iteration such that the endpoints of the segment that it is replacing and the endpoints of the generator match.

The iterative process of replacing each segment is continued for every new shape. For a true fractal, this process is repeated an infinite number of times.

From the explanation above regarding the length of the generator versus the length of the straight segment that it is replacing, it can be seen that the endpoints of the starting shape do not ever move. The five iterations shown in Figure 5.2 are all drawn on the same scale. It can clearly be seen that the volume occupied by the shapes is not increasing as the number of iterations increase. However, each iteration increases the total perimeter of the shape by one third.

5.1.2 Antenna Analysis

To utilize the fractal loop as an antenna, an approximation must be made. A true fractal, with an infinite perimeter, is physically impossible to realize. However, the first several iterations can be used to show the benefits of using fractal geometries.

To show the benefits of a small fractal loop antenna, the fourth iteration of the Koch loop is compared to a circular loop antenna. The relative sizes of the two antennas are shown in Figure 5.3. It can be seen that the circular loop antenna circumscribes the fractal loop. However, the areas occupied by the two antennas are not the same. The circular antenna occupies a larger area.

The area of the fourth iteration of the fractal loop, which is a key parameter for small loop antennas, with a radius r, is given by

$$\text{Area}_{\text{Koch loop}} = \left(1 + \frac{3}{9} + \frac{12}{81} + \frac{48}{729} + \frac{192}{6561}\right)\frac{1}{2}\frac{3\sqrt{3}}{2}r^2 = 2.05r^2 \tag{5.1.1}$$

The area of a circle is given by

$$\text{Area}_{\text{Circular loop}} = \pi r^2 \tag{5.1.2}$$

Therefore, if the two areas are compared,

$$\frac{\text{Area}_{\text{Koch loop}}}{\text{Area}_{\text{Circular loop}}} = 0.65 \tag{5.1.3}$$

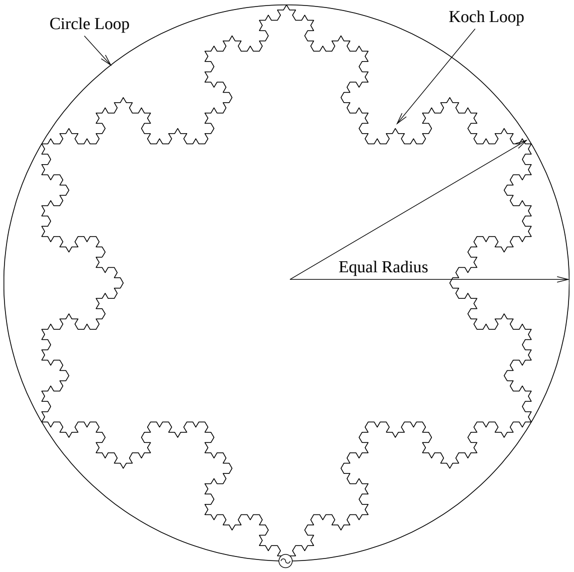

Figure 5.3: Relative sizes of the loop geometries. Volume occupied by both geometries is identical. The input source is shown at the bottom of the loops.

it can be seen that the area of the fourth iteration of the Koch island fractal is 35% smaller than a circumscribed circle.

The perimeter of the fourth iteration of a Koch loop is given by

$$\text{Perimeter}_{\text{Koch loop}} = 3\sqrt{3}r\left(\frac{4}{3}\right)^{n} \tag{5.1.4}$$

where n is the number of generating iterations. Therefore, the perimeter of a fourth iteration Koch loop is given by

$$\text{Perimeter}_{\text{Koch loop}} = 16.42r \tag{5.1.5}$$

The circumference of a circle is

$$\text{Perimeter}_{\text{Circular loop}} = 2\pi r \tag{5.1.6}$$

Therefore, the perimeter of a fourth iteration Koch loop is 2.6 times longer than a circumscribed circular loop.

$$\frac{\text{Perimeter}_{\text{Koch loop}}}{\text{Perimeter}_{\text{Circular loop}}} = 2.614 \tag{5.1.7}$$

The two antennas are analyzed using the moment method. The segment size for each of the antennas are identical. A frill voltage source is used to model the feed to determine the input impedance of the antenna. A delta gap source is used to model the feed to calculate the far field patterns. The location of the feed is shown in the bottom of Figure 5.3.

The antennas are tested over a frequency range that has been normalized to the length of the perimeter of the circular loop. The circular loop antenna has a perimeter of 0.05 λ to 0.26 λ over the tested frequency range. The perimeter of the fractal loop is 0.13 λ to 0.68 λ. For this range, the segment length for the simulations span 0.00017 λ to 0.00089 λ, while the wire diameter ranges from 0.000014 λ to 0.000072 λ.

5.1.3 Results

The moment method is used to calculate the input resistance and the far field pattern of the two antennas. Their results are compared below.

The input resistance of the two antennas are compared in Figure 5.4. A circular loop with a perimeter of 0.05 λ has an input resistance of 0.000004 Ω, increasing to only 1.17 Ω as the perimeter increases to 0.26 λ. However, the input resistance of the fractal loop increases at a much higher rate than the circular loop. The input resistance at the low end of the tested range is still very low, 0.000015 Ω, but increases to 26.65 Ω at the higher end of the range. The input resistance of a fractal loop and a circumscribed circular loop is plotted in Figure 5.4 versus the perimeter of the circular loop in wavelengths. The noise in the plots are from numerical limitations due to the small sub-sectioning of the structures.

The small input impedance matches the prediction of the radiation resistance given in [44]. Thus, ignoring ohmic losses, the radiation resistance for a small loop at the upper end of the test range is given by

$$R_r \simeq 31,171\left(\frac{S^2}{\lambda^4}\right) = 0.9\Omega \tag{5.1.8}$$

where S is the area enclosed by the loop, $\pi(0.0414\lambda)^2$. This matches closely with the value of 1.17 Ω that was calculated with the moment method.

The improvement of the input resistance of a fractal loop creates a better

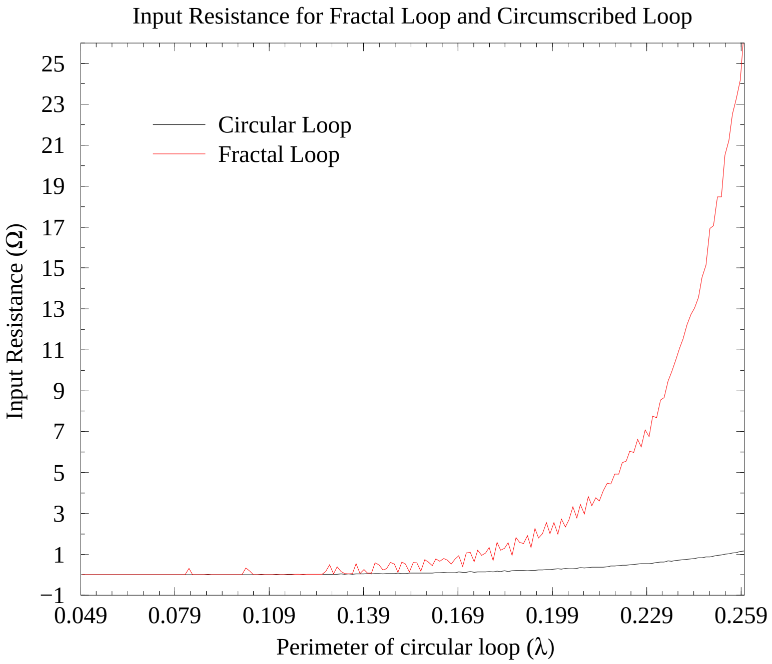

Figure 5.4: Simulated real part of the input impedance for the loop antennas.

match between the loop antenna and a 50 Ω transmission line. An input resistance of 26 Ω allows for an input match better than S11 = -10 dB. There is an imaginary component in the input impedance of the antennas which would increase the mismatch losses. However, theoretically, a reactive element can be added in parallel to the antenna to make it resonant.

The far field pattern for the two loops are compared in Figure 5.5. Figure 5.5 (a) shows the patterns in the xz and yz cuts. Figure 5.5 (b) plots the pattern in the xy plane. The loops are in the xy plane.

The simulated directivity of the circular loop antenna is 1.63 dB, while the simulated directivity of the fractal loop antenna is 1.53 dB. The simulated directivity of the small circular loops matches well with the predicted value of

$$D_0 = 4\pi \frac{U_{\text{max}}}{P_{\text{rad}}} = \frac{3}{2} = 1.76 \text{ dB} \tag{5.1.9}$$

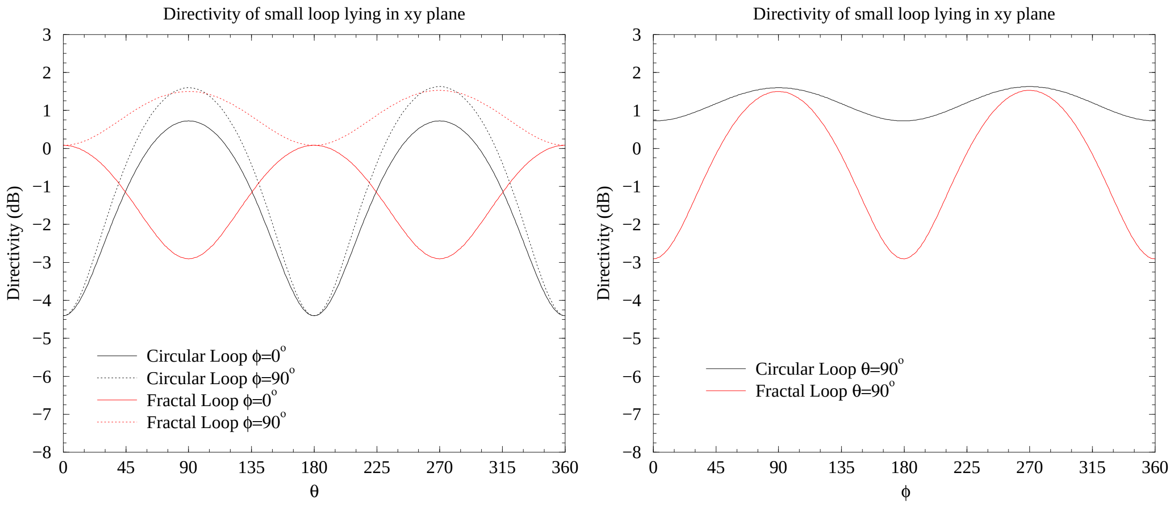

(a) (b)

Figure 5.5: Simulated far field patterns for loop antennas lying in xy plane. a) xz and yz cuts b) xy cut.

given in [44], where $U_{\max}$ is the maximum radiation intensity and P_{rad} is the total power radiated.

The effective aperture size for this type of antenna is given in [44] as

$$A_{em} = \left(\frac{\lambda^2}{4\pi}\right) D_0 = \frac{3\lambda^2}{8\pi} = 0.119\lambda^2 \tag{5.1.10}$$

The aperture efficiency for the circular loop antenna is given by,

$$\frac{A_{em}}{S} = \frac{0.119\lambda^2}{\pi\left(0.0414\lambda\right)^2} = 22.12 \tag{5.1.11}$$

This shows that the circular loop antenna is 22 times larger electrically than its physical size.

For the fractal loop antenna, the effective aperture is

$$A_{em} = \left(\frac{\lambda^2}{4\pi}\right) D_0 = 0.113\lambda^2 \tag{5.1.12}$$

which results in an aperture efficiency of

$$\frac{A_{em}}{S} = \frac{0.113\lambda^2}{2.05\,(0.0414\lambda)^2} = 32.21 \tag{5.1.13}$$

Therefore, electrically the fractal antenna is 32 times larger than the area it encompasses.

It is interesting to note that the directivity levels of the loop antennas are very similar to each other. However, because the length of the fractal is closer to one wavelength, 0.68 λ, the radiation patterns are not similar. The radiation pattern of a typical small loop is very similar to a small dipole. As the perimeter gets longer, the pattern begins to develop a multi-lobe pattern. Due to the increased length of the perimeter of the fractal antenna, the multi-lobe pattern emerges before it would for a circular loop even though the area of the fractal antenna is smaller than that of a circular loop.

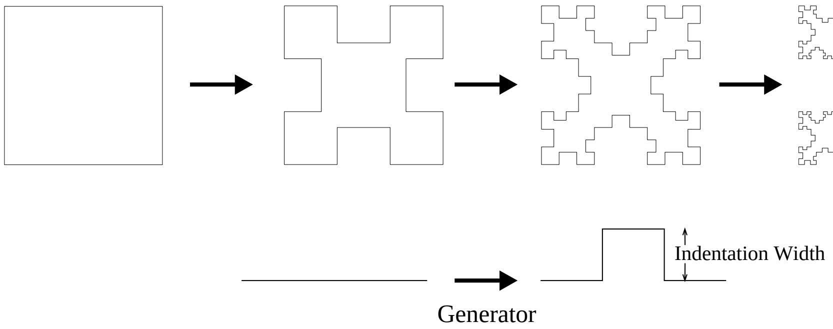

Figure 5.6: Sequence for generating a Minkowski loop. Each iteration is generated by replacing each segment of the previous iteration with the generator.

5.2 Resonant Loops

The closer the perimeter of a loop antenna gets to one wavelength, the more dependency its characteristics have on the shape in addition to its size. A fractal shape can be used to reduce the size of the antenna by increasing the efficiency with which it fills up its occupied volume with electrical length.

A Minkowski fractal is analyzed, where the perimeter length is near one wavelength. Several iterations are compared with a square loop antenna to illustrate the benefits of using a fractal antenna.

5.2.1 Fractal Generation

The fractal shape that is studied in this class of fractal loop antennas is a square Minkowski loop. The generation of the fractal is very similar to the loop that was used in the previous section. The fractal used in the small loop section was a Koch loop started with a triangle. A square is the starting shape for this fractal. The process is outlined in Figure 5.6.

A similar sequence is utilized in the generation of this loop as for the small loop. A generator segment replaces each segment in the starting shape. The starting shape is a square. Each of the four sides is replaced with the generator, shown in the bottom of Figure 5.6. The generator is scaled after every iteration such that the endpoints of the generator are exactly the same as the starting line segment.

This process of replacing every segment with the generator is repeated an infinite number of times in the generation of a true fractal. The starting square shape has an iteration number of 0. Replacing each of the four sides of the starting square with the generator is the first iteration. Replacing every segment of the new shape with the generator is the second iteration, and so on.

In the section covering small fractal loops, each segment of the generator had the same length, one third of the original length. For the square fractal for this section, the length is variable. The two end segments and the middle segment are $\frac{1}{3}$ of the starting segment length. The other two segments are tuned to adjust the overall perimeter of the fractal length. This tuning length is called the indentation width and is labeled on the generator shown in the bottom of Figure 5.6.

Varying the indentation width affects the fractal dimension of the shape. The greater the indentation width, the greater the fractal dimension. The fractal dimension dictates the space filling ability of the fractal. A dimension of 1.0 only fills up one dimension. Likewise, a dimension of 2.0 completely fills up a two dimensional area. As the dimension approaches two, the more it fills up a planar area. Therefore, the area encompassed by the fractal loop and the overall perimeter length is dependent on the indentation width.

5.2.2 Antenna Analysis

This fractal is analyzed as a resonant loop antenna by analyzing a finite number of iterations. The first two iterations of the antenna, as well as a square antenna, are compared to show how the characteristics of the antennas change as the number of iterations are increased.

The fractal shape is also varied by the indentation width. Six representative widths were chosen. They include: $\frac{1}{5}$, $\frac{1}{3}$, $\frac{1}{2}$, $\frac{2}{3}$, $\frac{4}{5}$, and $\frac{9}{10}$. The indentation widths are the widths of the second and fourth segments as a fraction of the other three lengths, which were each $\frac{1}{3}$ the length of the starting segment, as depicted in the bottom of Figure 5.6.

The antennas are simulated using the moment method and verified by fabricating and testing representative variations in a far field measurement chamber at the Antenna Laboratory at UCLA.

The antennas are all scaled by varying the starting overall width to be resonant at the same frequency. The segment length of each of the antennas are the same for each group with matching indentation widths. The size of the segment for each of these groups was determined by the smallest dimension of the highest iteration. The wire diameter for the simulations is 0.002 λ.

A voltage frill source is used to calculate the input impedance of the loop antennas while a delta gap source is used to model the feed in the far field calculations.

5.2.3 Design Curves

These antennas can be designed from the empirical data gathered while making the antennas resonant at the same frequency. The empirical data leads to design curves, which specify the starting width of the fractal for a particular indentation width and a particular fractal iteration.

The scaling factor that is used to scale a square loop with a width of $\lambda/4$ to

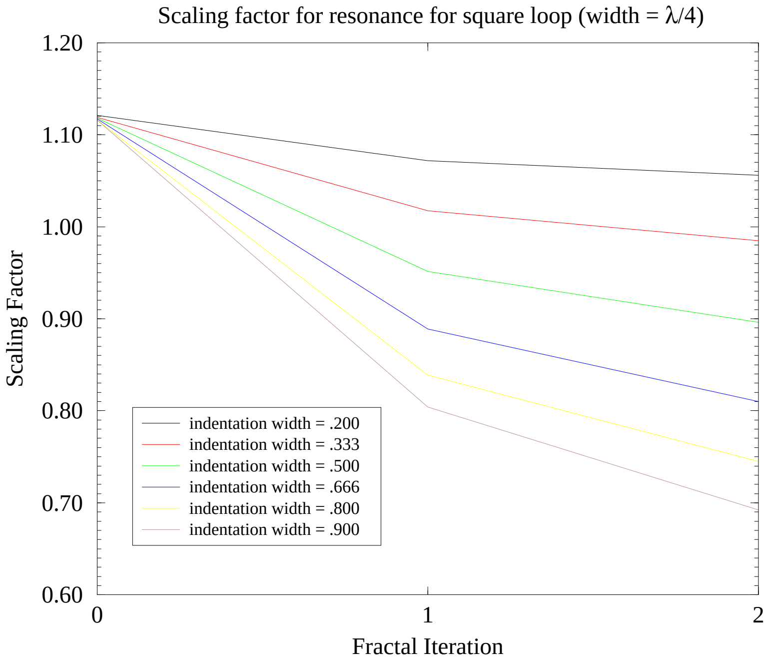

Figure 5.7: Scaling factor to make a square loop that is $\lambda/4$ per side resonant for different indentation width values for a Minkowski fractal loop.

achieve resonance for the various indentation widths versus the fractal dimension is shown in Figure 5.7.

It can been seen from these plots that as the indentation width is increased, the antennas are miniaturized more effectively. The fractal dimension is also directly related to the indentation width. While it is mathematically challenging to numerically define the fractal dimension of the loop, it is known that as the indentation width is increased, the fractal dimension is also increased. Therefore, one can suspect that higher fractal dimensions lead to better miniaturization of resonant loop antennas.

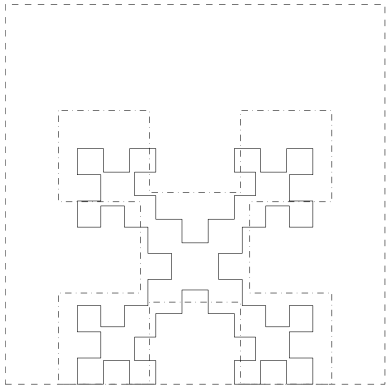

Figure 5.8: Relative sizes of the loop geometries for the first two iterations with an indentation width of 0.8. Each loop shown is resonant at the same frequency.

5.2.4 Results

Loops that have the same resonance with an indentation width of 0.8 are shown relative to each other in Figure 5.8. It can be seen how the second iteration loop is much smaller than the square loop.

The required heights of each of the loops to be resonant was determined by the moment method and verified by building and measuring the antennas. The height of each of the loops versus the fractal iteration is given in Figure 5.7 for various indentation widths. The input match of these antennas at resonance vary between 100 Ω down to 40 Ω.

The far field patterns for the square loops of different indentation widths and fractal iterations are shown in Figure 5.9. The pattern is the yz cut. The loop antenna lies in the xz plane.

The directivities of the loop antennas are given in Table 5.1 along with their relevant geometrical properties. The calculated directivity of the square loop, 3.45 dB, compares with the expected max directivity for a one-wavelength square loop given in [45] of 3.09 dB. The directivities of the fractal loops are slightly lower

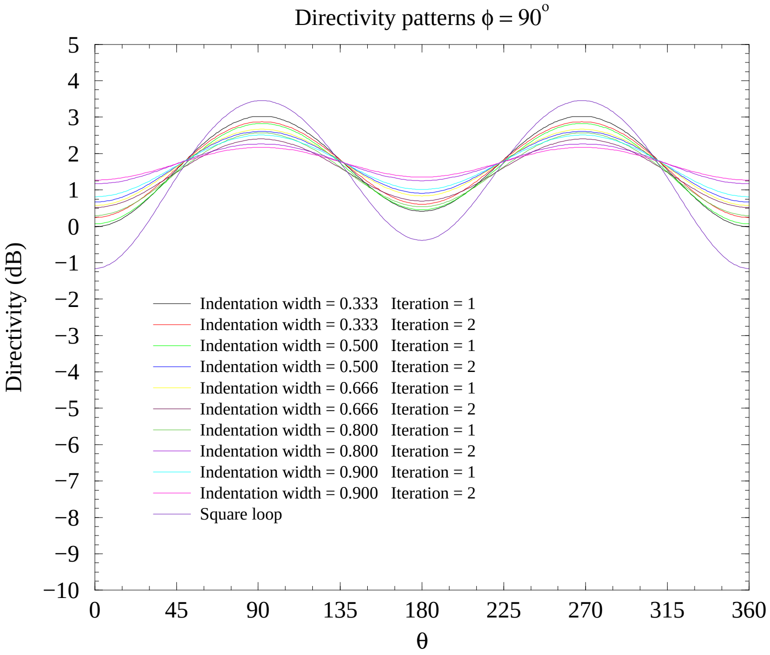

Figure 5.9: Far field pattern for resonant fractal loop antennas for various indentation widths and fractal iterations as computed by the moment method. The pattern cut is orthogonal to the plane of the loop.

than that of a square loop. The directivities of the fractal loops range from 3.21 dB for the lowest iteration fractal loop with the shallowest indentation width to 2.17 dB for the fractal loop with the highest iteration and largest indentation width.

Table 5.1: Directivity data for the loop antennas over varying indentation widths and fractal iterations. All of the antennas are resonant at the same frequency.

Indentation	Iteration	Width	Area	D_o (dB)	A_{em}	A_{em}/S
0.200	1	0.2680λ	$0.06543\lambda^2$	3.21	$0.1666\lambda^2$	2.547
	2	0.2640λ	$0.06005\lambda^2$	3.12	$0.1632\lambda^2$	2.718
0.333	1	0.2543λ	$0.05510\lambda^2$	3.02	$0.1595\lambda^2$	2.895
	2	0.2462λ	$0.04665\lambda^2$	2.87	$0.1541\lambda^2$	3.303
0.500	1	0.2379λ	$0.04400\lambda^2$	2.82	$0.1523\lambda^2$	3.462
	2	0.2240λ	$0.03284\lambda^2$	2.61	$0.1451\lambda^2$	4.420
0.666	1	0.2222λ	$0.03477\lambda^2$	2.66	$0.1468\lambda^2$	4.223
	2	0.2025λ	$0.02212\lambda^2$	2.40	$0.1383\lambda^2$	6.252
0.800	1	0.2097λ	$0.02833\lambda^2$	2.56	$0.1435\lambda^2$	5.064
	2	0.1862λ	$0.01549\lambda^2$	2.27	$0.1342\lambda^2$	8.662
0.900	1	0.2010λ	$0.02423\lambda^2$	2.51	$0.1418\lambda^2$	5.853
	2	0.1731λ	$0.01132\lambda^2$	2.17	$0.1312\lambda^2$	11.59
Square	0	0.2795λ	$0.07812\lambda^2$	3.45	$0.1761\lambda^2$	2.254

It is interesting to point out that even though the directivity decreases as the fractal iteration and indentation widths are increased, the aperture efficiency increases. The physical area encompassed by a fractal generated with a high number of iterations and with a deep indentation width is much smaller than a square loop. Therefore, while the aperture efficiency of a square loop is only 2.254,

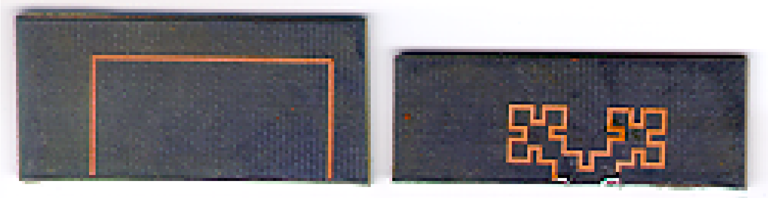

Figure 5.10: Fabricated loop antennas. The loop antenna was mounted over a ground plane. Both antennas are resonant at the same frequency.

the aperture efficiency of a second iteration fractal loop with a 0.9 indentation width has a aperture efficiency of 11.59. Comparing these two antennas, a loss of directivity of 1.28 dB can be traded off for a 38% decrease in occupied width, which correlates to an encompassed area that is almost 7 times smaller.

The antennas were fabricated using the techniques outlined in chapter 4. They are designed for resonance at 2.5GHz, a frequency that is in common use in wireless applications, and easily measurable and manufacturable. Photographs of the resulting antennas are shown in Figure 5.10 and Figure 5.11. Figure 5.10 shows the antennas that were attached over a ground plane using image theory as the other half of the loop. The antennas in Figure 5.11 are fabricated using the microstrip to co-planar strip method that was described in chapter 4.

The resulting input matches of the fabricated antennas of Figure 5.10 are plotted in Figure 5.12. The input match is in reference to 50 Ω and has been measured using an HP 8510B network analyzer.

The calibrated far field patterns of the same antennas are shown in Figure 5.13. The patterns are taken in a cut that is orthogonal to the plane of the loop. It can be seen that the resulting gains of the antennas are very similar to those predicted with the moment method simulations. The asymmetry in the patterns is due to reflections off of the walls of the chamber. These reflections result from measuring the antennas at the limits of the allowable frequency range

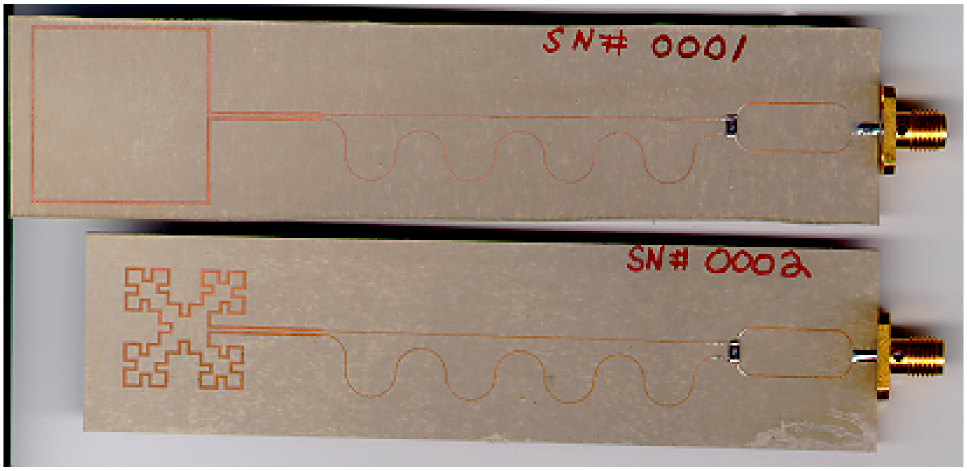

Figure 5.11: Fabricated loop antennas using a microstrip to co-planar strip transition. Both antennas are resonant at the same frequency.

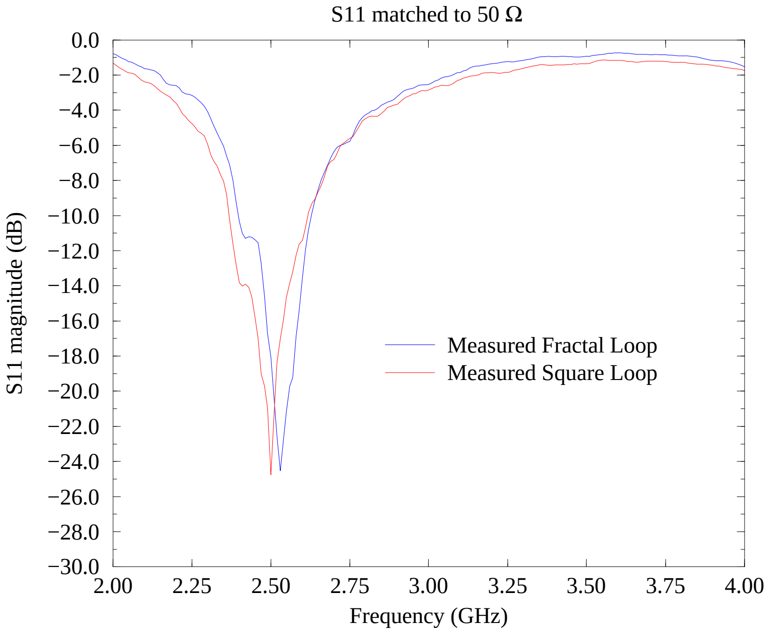

Figure 5.12: Input match for fabricated loop antennas. The shift in resonant frequency is from the dielectric backing.

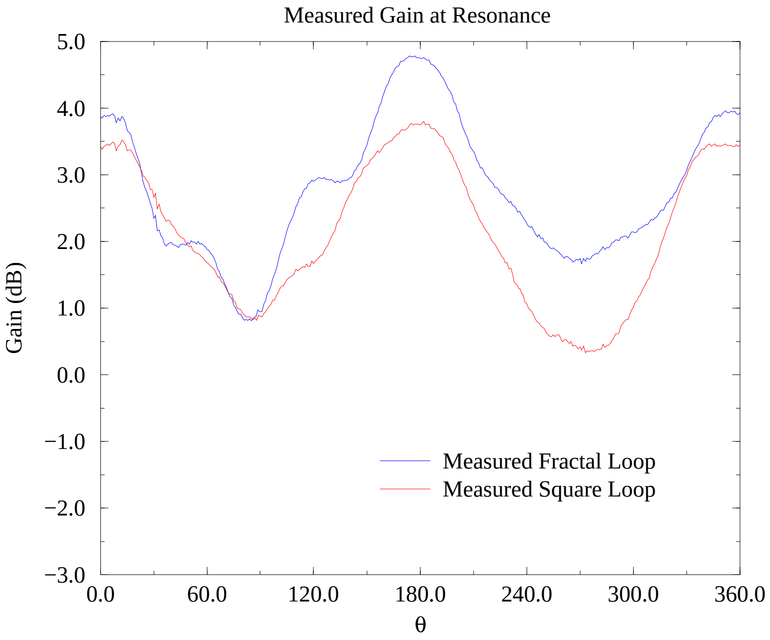

Figure 5.13: Measured far field pattern for the loop antennas at resonance. The patterns are calibrated for an accurate gain measurement.

of the microwave absorbers used to line the chamber.

The input match and the far field patterns of the antennas fabricated using the CPS-to-microstrip technique, pictured in Figure 5.11, are very similar to the data shown above.

CHAPTER 6

Fractal Dipole Antennas

The previous section showed the benefits of fractal loop antennas. Dipoles can benefit from fractal geometries, as well. The expected benefit of using a fractal as a dipole antenna is to miniaturize the total height of the antenna at resonance, where resonance means having no imaginary component in the input impedance.

In the next several sections three types of fractals are investigated as dipole antennas. They include two planar structures, a Koch curve and a fractal tree, and a three dimensional fractal tree. These three types of fractals are compared among each other and to a straight dipole.

These antennas are simulated as dipoles along the z axis using the moment method. The starting structure for each of these fractal geometries is straight dipole that is resonant in the PCS band, at 1900 MHz. In the simulations, the antenna height is held constant and the frequency is swept. It can be seen that the resonant frequency decreases as the number of fractal iterations increases. The decrease in resonant frequency can correlate to a miniaturized antenna, if the resonant frequency would be held fixed.

6.1 Koch Monopole

The first fractal shape that is investigated as a dipole antenna is the Koch curve. The geometry of how this antenna could be used as a dipole is shown in Figure 6.1.

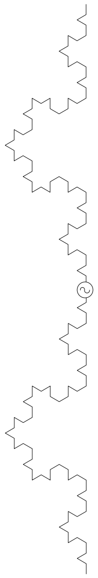

Figure 6.1: Geometry of a Koch curve used as a dipole antenna.

This type of fractal has been previously studied in [25]. Similarly, in this thesis, the goal of using a Koch curve as a dipole is the miniaturization of the antenna at resonance.

6.1.1 Fractal Generation

A Koch curve is generated by replacing the middle third of each straight section with a bent section of wire that spans the original third as shown in Figure 6.2.

Each iteration adds length to the total curve. This can be seen from the figure depicting the generating process. Each iteration results in a total length that is 4/3 times the original geometry. However, the overall height of the fractal does not change from one iteration to the next. Therefore, if the process is carried out for an infinite number of times, the curve would have an infinite length while the overall height would not change.

The total length of the Koch curve is given by

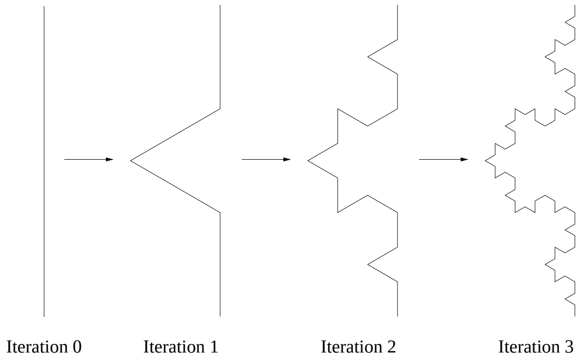

Figure 6.2: First iterative steps for generating a Koch curve.

$$\text{Length}_{\text{Koch}} = h\left(\frac{4}{3}\right)^{n} \tag{6.1.1}$$

where n is the number of iterations and h is the height of the straight starting generator.

The starting structure that is used in this section is half of a resonant PCS dipole, which is 3.75 cm in length. The overall length of the resonant dipole is 7.5 cm, which is slightly smaller than $\lambda/2$ at 1900 MHz.

6.1.2 Antenna Analysis

These fractals are analyzed as resonant dipole antennas using the moment method. The fractal generated in the previous section is mirrored at its base and fed as a dipole as depicted in Figure 6.1. The first five iterations of the Koch fractal are analyzed. By observing the first five iterations, the benefits of using fractal geometry will become apparent while avoiding the difficulties of simulating structures with very complex geometries. It can be shown that the benefits of fractal antennas begin to diminish as the number of generating iterations is increased beyond the first few. These first five iterations are compared with a straight dipole, iteration 0.

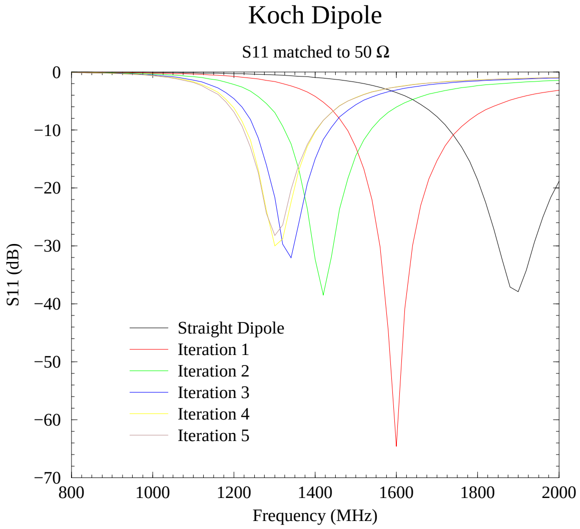

Figure 6.3: Simulated input match of the straight dipole and the first five iteration for the Koch dipole antennas matched to 50 Ω.

All of these antennas are subsectioned with equally sized segments. Each subsection is 0.000977 λ in length and 0.00095 λ in diameter, where λ is the wavelength at 1900 MHz. For the input impedance calculations, a frill voltage source is used, while a delta gap voltage source is used in far field calculations.

6.1.3 Antenna Characteristics

The simulated characteristics of the Koch dipole are presented in this section. In Figure 6.3, the input impedances of the dipoles are plotted versus frequency. It can be seen how the resonant frequency drops as the number of generating iterations for the fractal is increased. Also, it is interesting to note that the resonant frequency approaches an asymptotic limit. This limit gives an insight into where the resonance of an ideal Koch fractal curve as a dipole would lie, if such a structure were manufacturable. The simulated input impedance plots are shown in Figure 6.4.

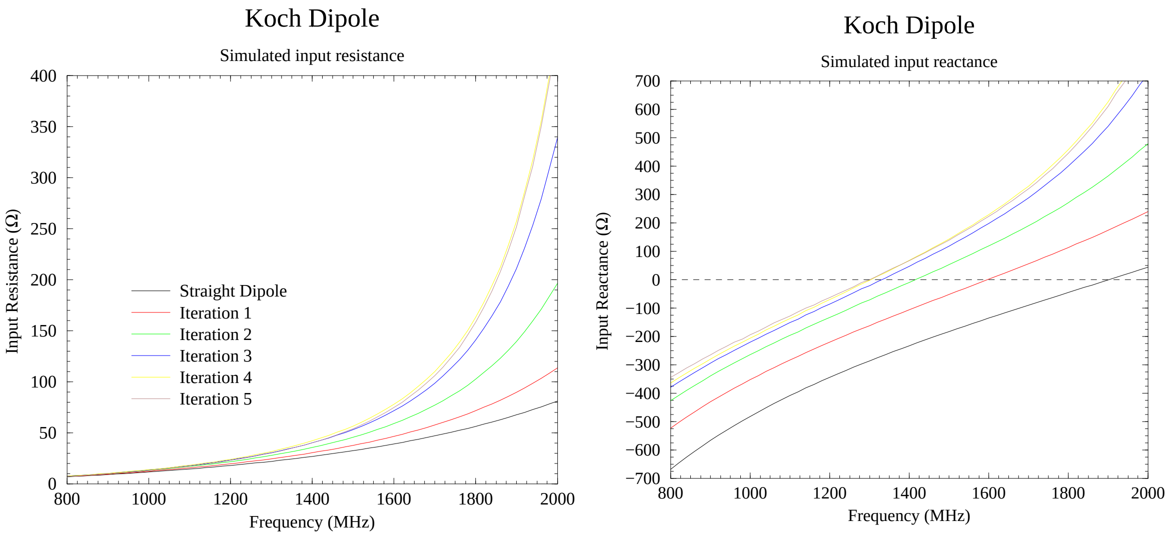

(a) (b)

Figure 6.4: Simulated input impedance for the first five fractal iterations of Koch dipoles plus a straight dipole for comparison. a) Input resistance b) Input reactance

The far field patterns for the different iterations are plotted in Figure 6.5 in all three primary cuts. The plots are all taken at resonance.

6.1.4 Iteration Scaling

The miniaturization of the fractal antenna is exhibited by scaling each iteration to be resonant at the same frequency. The relative heights of each iteration are plotted in Figure 6.6.

The miniaturization of the antennas shows a greater degree of effectiveness for the first several iterations. The amount of scaling that is required for each iteration diminishes as the number of iterations increase.

The geometrical results of the simulations are given in Table 6.1. The resulting total length of the resonant antennas show that the resonant frequency is not only

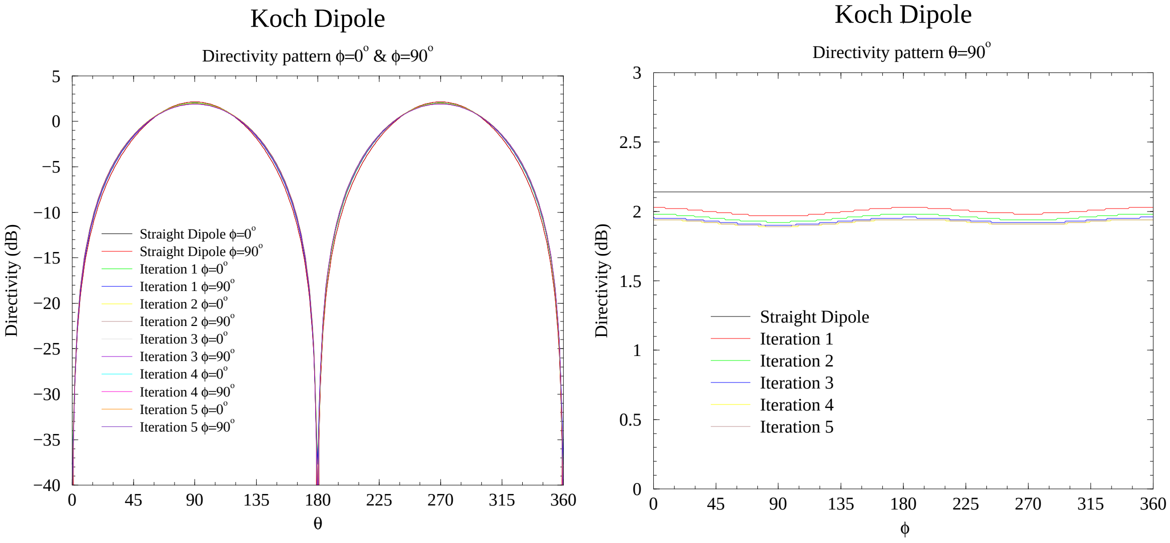

(a) (b)

Figure 6.5: Far field directivity pattern for Koch dipoles of different fractal iterations. a) versus θ for $\phi = 0^o$ and $\phi = 90^o$, b) versus ϕ for $\theta = 90^o$

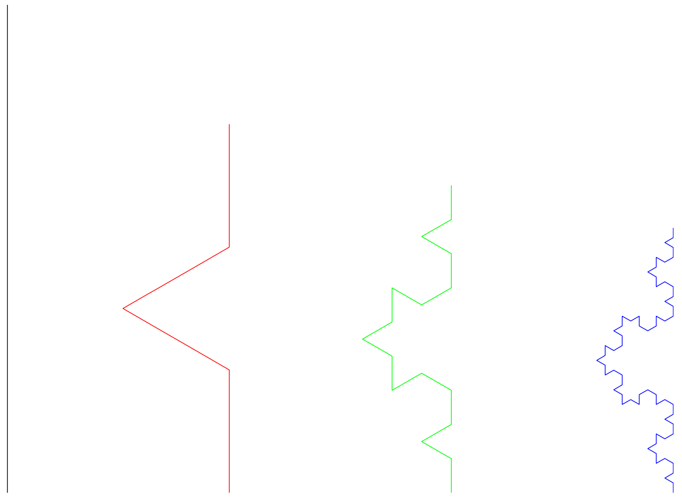

Figure 6.6: Relative heights of a resonant Koch dipole for different fractal iterations. Only half of the dipole is shown in the figure.

Table 6.1: Height and length of Koch fractal antennas in terms of wavelengths at resonance.

Iteration	Height	Length
0	0.475 λ	0.475 λ
1	0.399 λ	0.532 λ
2	0.354 λ	0.629 λ
3	0.332 λ	0.788 λ
4	0.326 λ	1.029 λ
5	0.324 λ	1.367 λ

a function of the electrical length. The total length of the fractals at resonance is increasing, while the height reduction is reaching an asymptote. Therefore, it can be concluded that the increased complexity of the higher iterations are not advantageous. The miniaturization benefits are achieved in the first several iterations.

6.2 Fractal Tree

Another type of fractal that can be utilized as a dipole is a fractal tree. The geometry of how the fractal is used is shown in Figure 6.7. This deterministic fractal is a simple model of branching found in nature. Again, the goal of using this type of fractal is to reduce the height of a resonant dipole antenna.

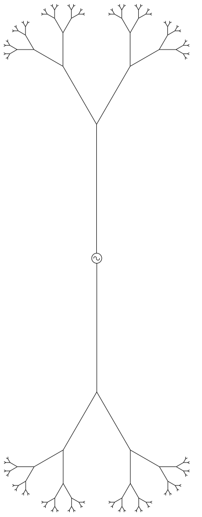

Figure 6.7: Geometry for the feeding of a fractal tree as a dipole.

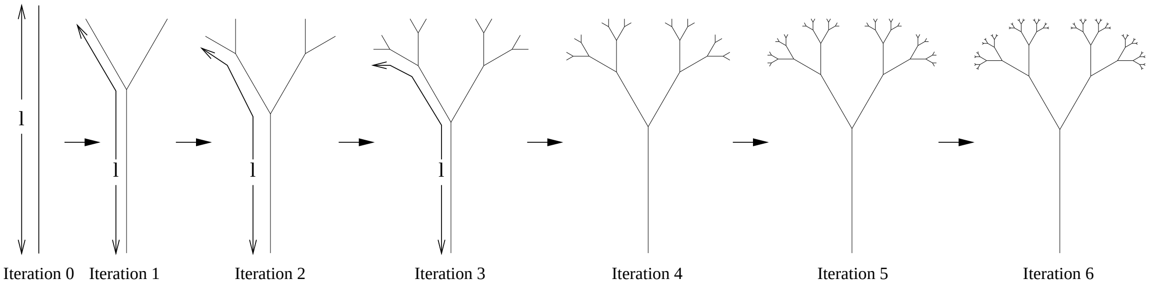

Figure 6.8: Geometry for the feeding of a fractal tree as a dipole.

6.2.1 Fractal Generation

The fractal is generated by applying an iterative sequence to the starting structure. The fractal is started with a simple monopole. The top segment of this monopole is then split at a pre-determined angle, $\theta = 60^o$ in this section, to form the first two branches. As the iterative process continues, the end segment of each branch splits into two more branches as shown in Figure 6.8.

The total electrical length of the conductor, l, which is depicted graphically in Figure 6.8, remains constant throughout the iterative process. The total electrical length can be defined as the shortest length from the base of the fractal to any other end.

The lengths of each straight section in the first five iterations are shown in Table 6.3. It can been seen from the section lengths that the total conductor length, l, always adds up to unity for each iteration.

Table 6.2: Length of each straight section of the fractal tree for the first five iterations.

Iteration	0	1	2	3	4	5
	1	$\frac{1}{3}$	$\frac{1}{7}$	$\frac{1}{15}$	$\frac{1}{31}$	$\frac{1}{63}$
		$\frac{2}{3}$	$\frac{2}{7}$	$\frac{2}{15}$	$\frac{2}{31}$	$\frac{2}{63}$
			$\frac{4}{7}$	$\frac{4}{15}$	$\frac{4}{31}$	$\frac{4}{63}$
				$\frac{8}{15}$	$\frac{8}{31}$	$\frac{8}{63}$
					$\frac{16}{31}$	$\frac{16}{63}$
						$\frac{32}{63}$

6.2.2 Antenna Analysis

The first five iterations plus a straight dipole were analyzed using the moment method. In the previous section describing the Koch dipole antenna, the overall height was maintained from iteration to iteration. For the tree fractal, the total length of the conductor path, l, is maintained among iterations. The fractal is mirrored at its base and fed in the center as dipole. This is depicted in Figure 6.7.

The subsection size for each iteration of the antenna is the same. The segments are each $1/63$ of the total conductor length l. At the resonant frequency of the straight dipole, 1900 MHz, this length is equal to $0.00377\ \lambda$. The diameter of

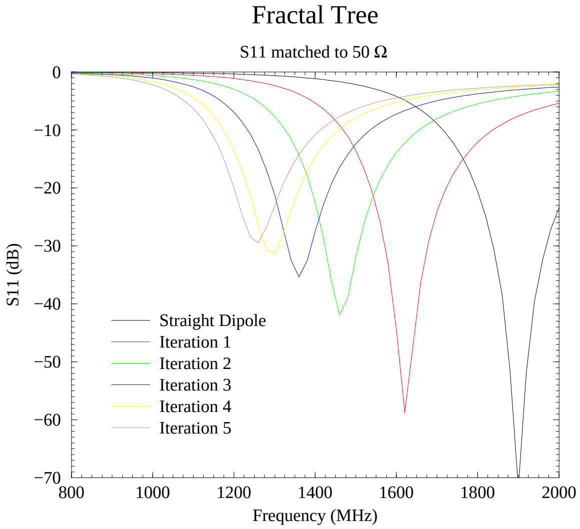

Figure 6.9: Simulated input impedance matched to 50 Ω for the first five iterations of a fractal tree dipole with a split angle of 60^o and for a straight dipole.

each segment is 0.00095 λ at this frequency.

Similar to the previous simulations, the feed is modeled as a frill voltage source for input impedance calculations and a delta gap for far field calculations.

6.2.3 Antenna Characteristics

The input match, compared to 50 Ω, of the fractal dipoles and straight dipoles as calculated using the moment method are shown in Figure 6.9. The input impedances, real and imaginary, are shown in Figure 6.10.

It can be seen that the resonant frequency drops as the fractal iteration is increased. The ratio of miniaturization versus the fractal iteration is very similar to that of the Koch dipole. This observation will be compared in a subsequent section.

As the fractal iteration is increased, the resonant frequency decreases in a saturating manner. At each iteration the extra number of branches top loads the

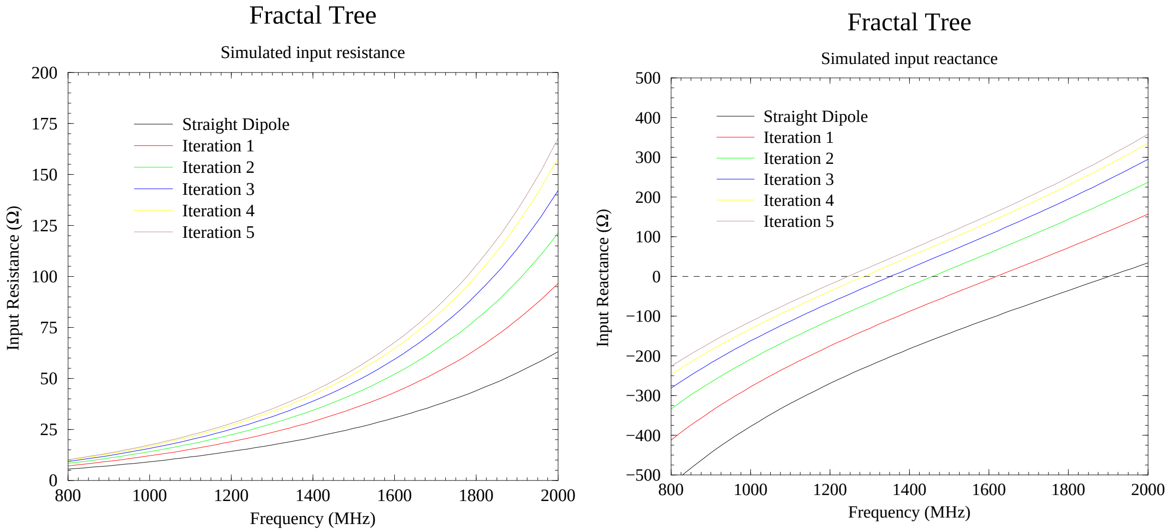

(a) (b)

Figure 6.10: Simulated input impedance for the first five iterations of a fractal tree dipole with a split angle of 60^o and a straight dipole. a) Input resistance, b) Input reactance

antenna. Even though the electrical length of a single conductor path from the generator port of the antenna to the tip of a branch is identical for all antennas, there are more branches after each iteration. This adds more conduction paths at the top of the antenna serving as a top-loading device. This, in turn, lowers the resonant frequency at every iteration. It can be seen that the top loading effect diminishes as the number of iterations is increased. The length of wire that branches out during each iteration is almost half as small as the previous iteration, thus the effect it has on the input characteristics of the antenna diminishes.

The far field patterns of a fractal tree dipole are very similar to that of a straight dipole in all cuts. A typical far field pattern of one of the antennas is shown in Figure 6.11. The antenna chosen with a typical far field pattern is a fourth iteration fractal tree whose branch split angle is 60^o.

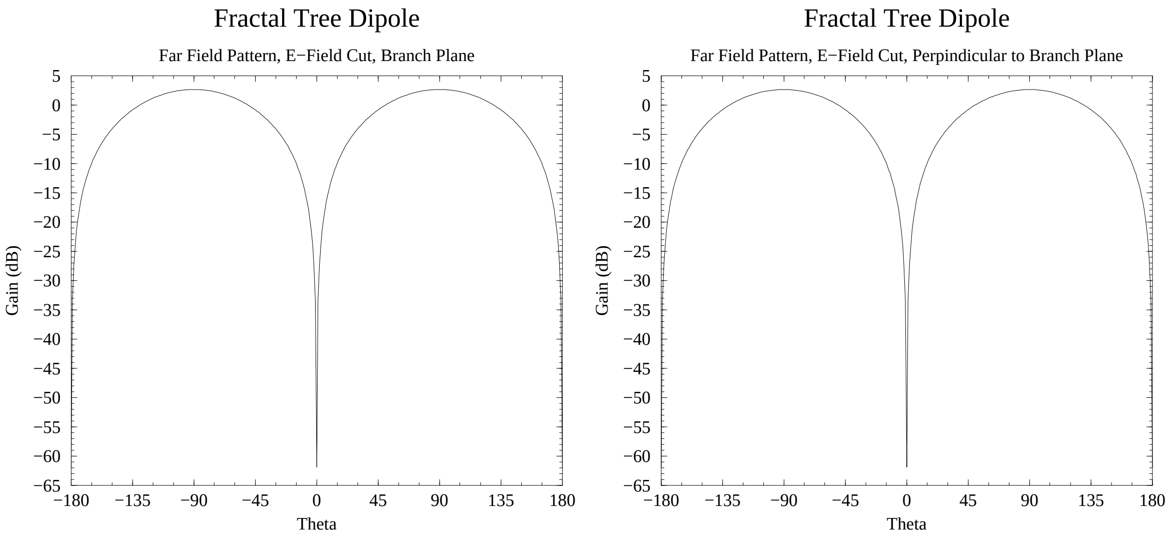

(a) (b)

Figure 6.11: Far field pattern of a typical fractal tree antenna. This one is for a fourth iteration fractal tree with a 60^o branch split. a) E-Plane cut that is parallel to plane of branches, b) E-Plane cut that is perpendicular to plane of branches

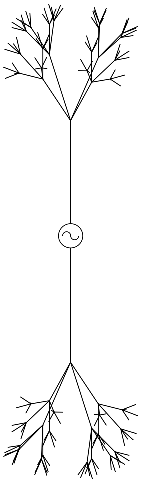

Figure 6.12: A three dimensional fractal tree fed as a dipole.

The benefit of using this class of fractal antennas is that it can miniaturize a standard dipole. The calculated far field patterns are very similar to a straight dipole antenna.

6.3 Three Dimensional Fractal Tree

A three dimensional fractal tree has a similar geometry as the previous section. However, instead of branching in one plane, the fractal branches out in three dimensions. The resulting antenna exhibits similar benefits as the two dimensional case to a greater degree. The geometry of how this type of fractal can be utilized as a dipole is shown in Figure 6.12

6.3.1 Fractal Generation

The three dimensional fractal tree is generated in a similar fashion as the two dimensional case. The top of a straight monopole is split into four branches. The

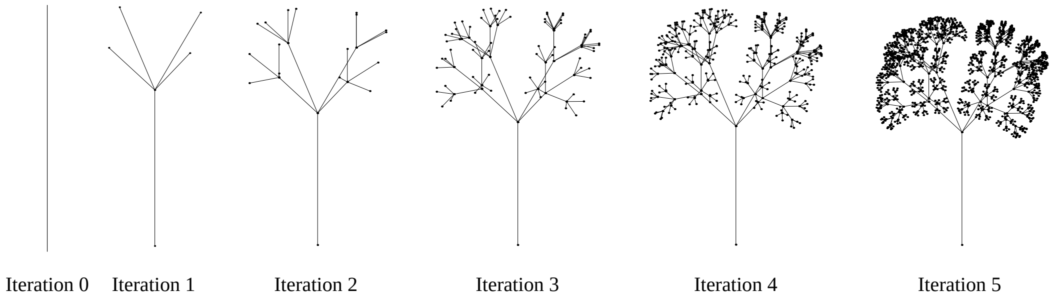

Figure 6.13: The generation of a three dimensional fractal tree. At each iteration the branches split into four segments in two orthogonal planes.

branches split off at a set angle in two orthogonal planes. The angle used in this study is 60^o. The resulting four branches then split in a similar manner. The ratio of the sizes of each of the branches at each iteration is outlined in Table 6.3. The generation of the first five iterations of the fractal is depicted in Figure 6.13.

Table 6.3: Length of each segment of the three dimensional fractal tree for the first five iterations.

Iteration	0	1	2	3	4	5
	1	$\frac{1}{3}$	$\frac{1}{7}$	$\frac{1}{15}$	$\frac{1}{31}$	$\frac{1}{63}$
		$\frac{2}{3}$	$\frac{2}{7}$	$\frac{2}{15}$	$\frac{2}{31}$	$\frac{2}{63}$
			$\frac{4}{7}$	$\frac{4}{15}$	$\frac{4}{31}$	$\frac{4}{63}$
				$\frac{8}{15}$	$\frac{8}{31}$	$\frac{8}{63}$
					$\frac{16}{31}$	$\frac{16}{63}$
						$\frac{32}{63}$

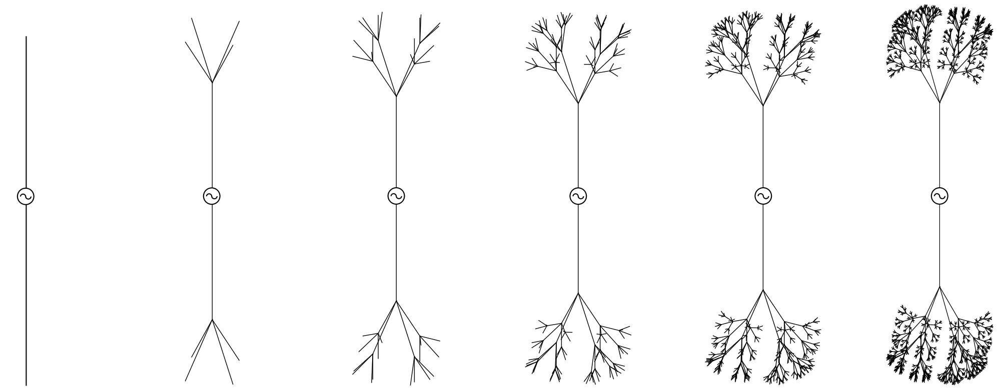

Iteration 0 Iteration 1 Iteration 2 Iteration 3 Iteration 4 Iteration 5

Figure 6.14: A dipole and the first five iterations of a fractal tree in a dipole configuration simulated using the moment method.

6.3.2 Antenna Analysis

For the purpose of studying this fractal as an antenna, the first five iterations are used. As before, this shows us the trends of the benefits of using a fractal within the computational limitations of the simulations. The fractal generated above is mirrored at the base. These antennas are simulated in a dipole configuration, as shown in Figure 6.14, using the moment method.

As in the two dimensional case, the subsection size for each iteration is the same. The segments have a length of $1/63\ l$, where l is still the length of a path from the base to one tip. At the resonant frequency of the straight dipole, 1900 MHz, the segment length is equal to $0.00377\ \lambda$. The diameter of each segment is $0.00095\ \lambda$ at this frequency.

Similar to the previous simulations, the feed is modeled as a frill voltage source for input impedance calculations and a delta gap for far field calculations.

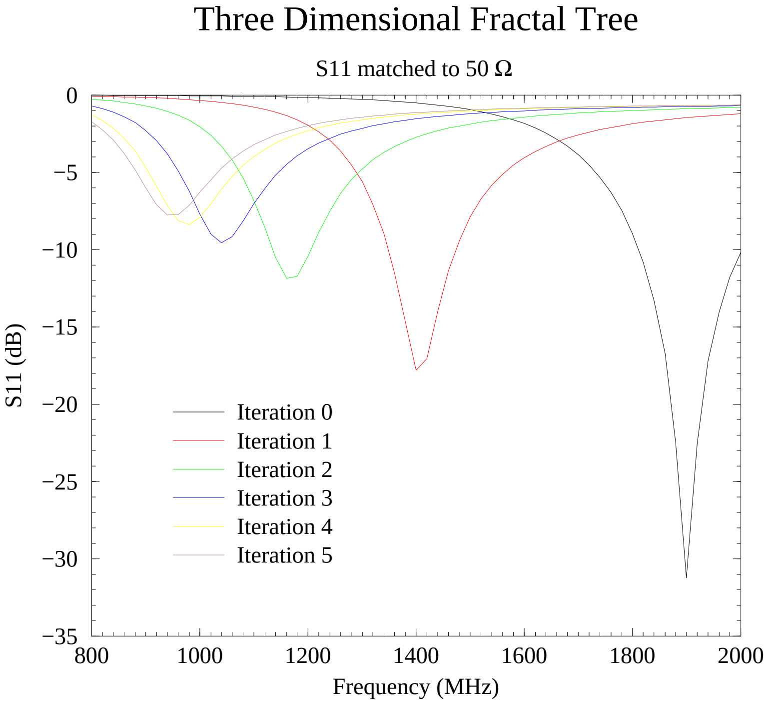

Figure 6.15: Input match for various iterations of a three dimensional fractal tree matched to 50 Ω.

6.3.3 Antenna Characteristics

The simulated input match for the antennas is shown in Figure 6.15. It can be seen how the resonant frequency decreases as the fractal iteration is increased. In a similar fashion as the previous fractal dipoles studied, the input resistance decreases as the fractal iteration is increased, resulting in a poorer input match.

The far field patterns of the fractal antennas are shown in Figure 6.16. The pattern is taken in a primary cut in the plane of the dipole. The dipole oriented along the z axis, this would be the $\phi = 0^o$ cut. The far field patterns of each of the iterations are calculated at resonance. It can be seen at resonance that the patterns do not vary as the fractal iteration is increased. In addition, the patterns and maximum directivities are very similar to the expected performance

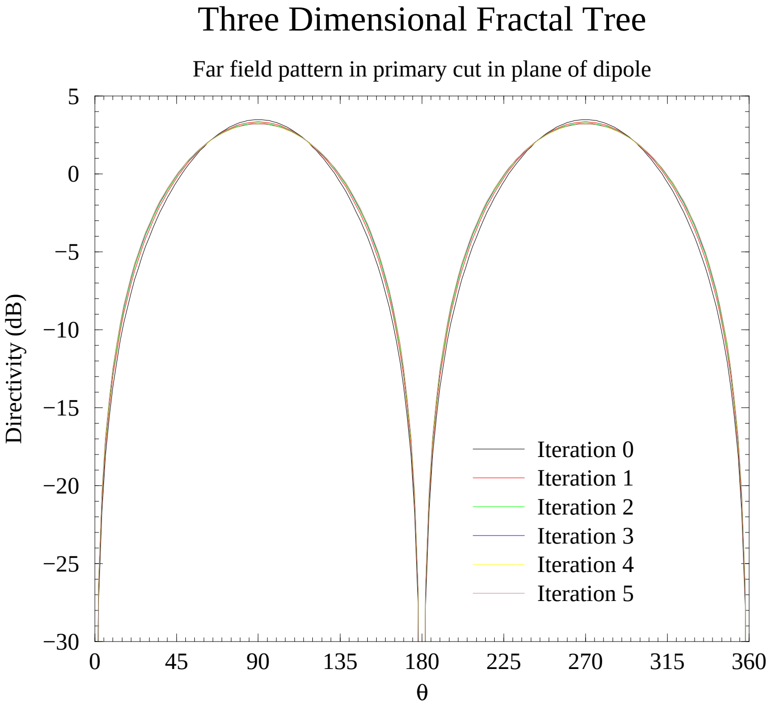

Figure 6.16: The simulated directivity patterns for the various iterations of the three dimensional fractal tree dipole. The pattern is taken in the $\phi = 0^o$ cut in the plane of the z directed dipole at resonance.

of the straight dipole.

6.4 Fractal Dipole Comparisons

The benefits of the various fractal geometries can be compared. All of the dipoles that are compared in this section have the same starting height. The starting geometry is a resonant dipole that is 7.5 cm in length, resonant in the PCS band at 1900 MHz. The relative geometry of all of the compared dipoles is shown in Figure 6.17.

The benefits of using a fractal geometry are dependent on the type of fractal that is chosen. A comparison of the miniaturization of the antennas by increasing

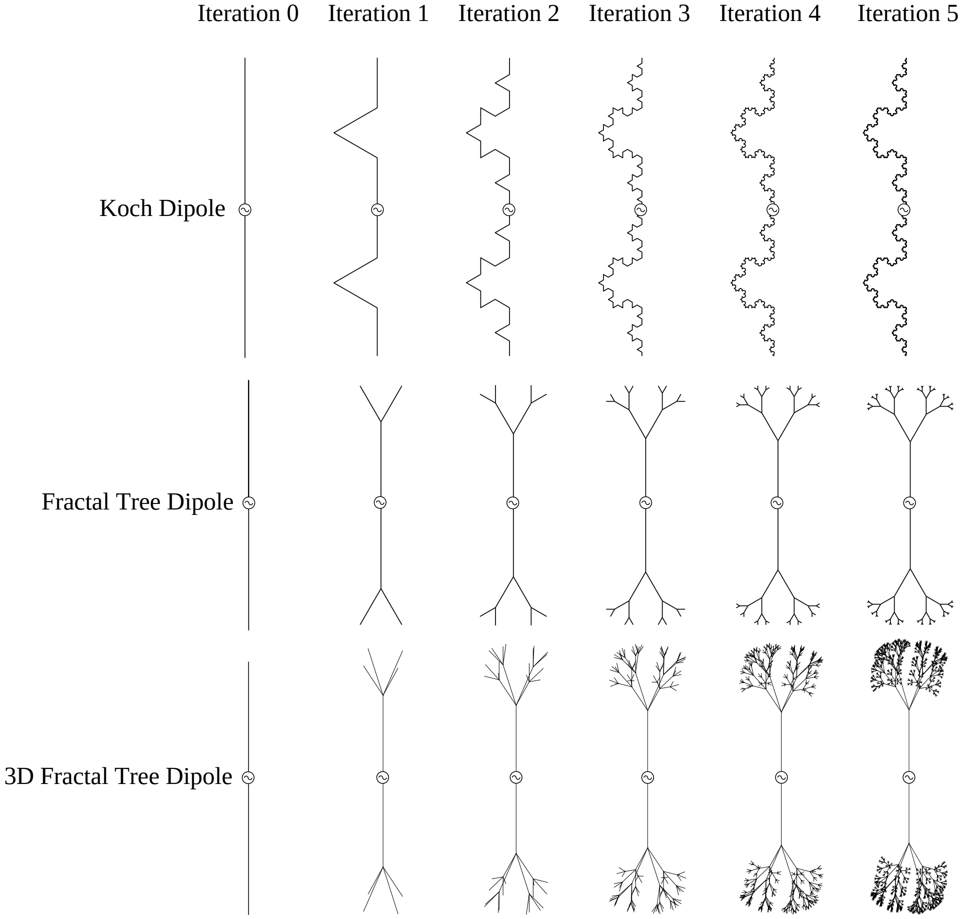

Figure 6.17: Three various fractal geometries are configured as dipoles, including a Koch fractal, a fractal tree, and a three dimensional fractal tree. The starting size of each of the geometries are identical PCS band dipoles.

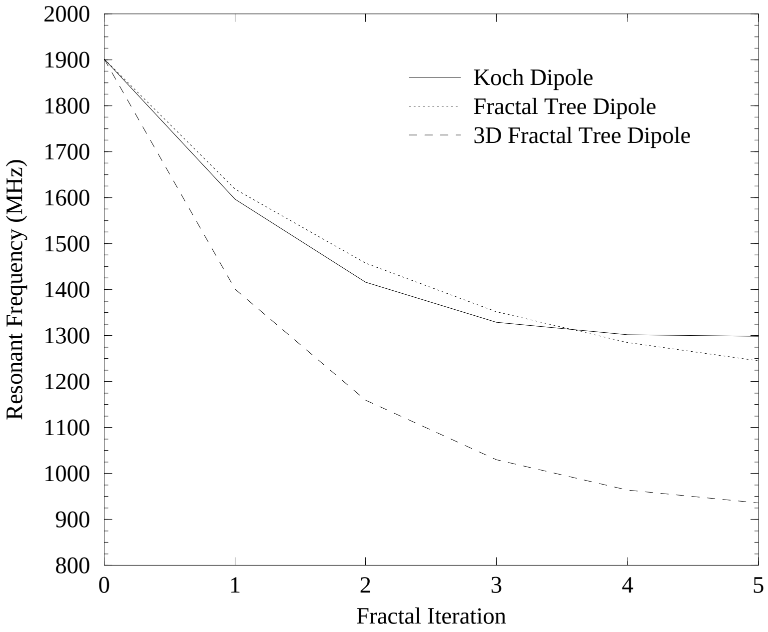

Figure 6.18: The resonant frequency for each of the fractal antennas versus the number of iterations for a Koch fractal, a fractal tree, and a three dimensional fractal tree in a dipole configuration as simulated with the moment method.

the number of generating iterations is depicted graphically in Figure 6.18.

It can be seen that the miniaturization benefits of both two dimensional structures, the Koch fractal and the fractal tree, are very similar. The benefit of the three dimensional fractal tree, however, is more pronounced.

Even though the three dimensional fractal miniaturizes the antenna at resonance to a greater degree than the other fractals, the input resistance is lowered by a significant amount, as well. It can be seen from Figure 6.19 that the input resistance of the Koch and fractal tree dipoles drops to near 30 Ω at resonance for the fifth iteration. Likewise, the input resistance of the three dimensional fractal tree drops to 20 Ω due to the increased amount of conducting branches. This would decrease the match to a 50 Ω feed line. The fractal geometry chosen

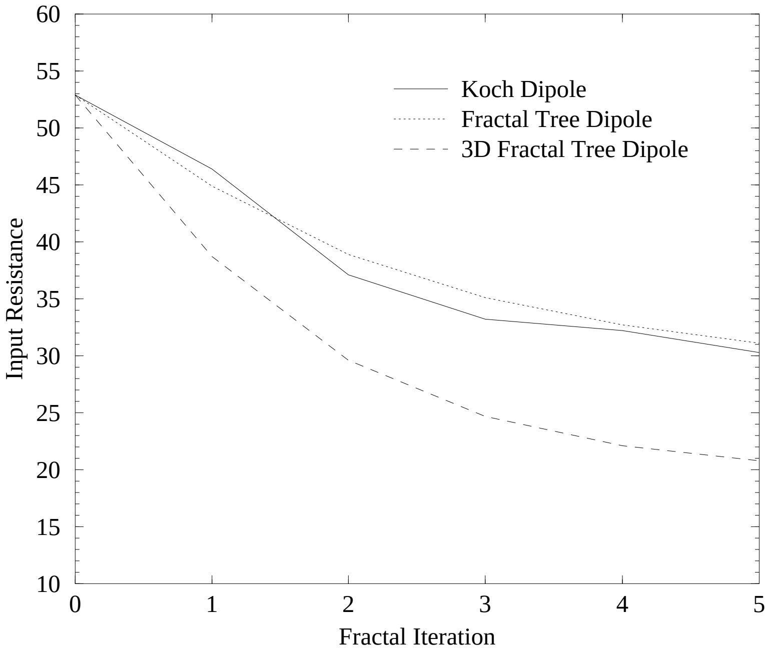

Figure 6.19: Simulated input resistance versus the number of generating iterations for three fractal antennas.

for a particular application would have to weigh the trade-off between increased miniaturization versus input resistance.

It can be seen from the plots of the simulated input match for the various dipoles that they are all narrow band antennas. The simulated 3 dB bandwidth of the dipole antenna is about 2.4%. This can be compared with the 3 dB bandwidth of the simulated fractals generated from the highest number of iterations, which have the lowest resonant frequency. The simulated bandwidth for the highest iteration of the Koch dipole is around 3.1%. For the fifth iteration of the fractal tree dipole, the simulated bandwidth is 4.2%. The simulated bandwidth of the fifth iteration of the three dimensional fractal tree is 12.7%, but only has a -7.75 dB input match at resonance.

CHAPTER 7

Multiband Fractal Antennas

So far, only the space saving benefits of fractal antennas have been exploited. There is another property of fractals that can be utilized in antenna construction. Fractals have self-similarity in their geometry, which is a feature where a section of the fractal appears the same regardless of how many times the section is zoomed in upon. Self-similarity in the geometry creates effective antennas of different scales. This can lead to multiband characteristics in antennas, which is displayed when an antenna operates with a similar performance at various frequencies.

The object of this chapter is to show how fractals can be used as multiband antennas. The Sierpinski sieve fractal is chosen as the geometry to test this feature due to its astounding similarities in performance as an antenna at various frequencies. This type of fractal as an antenna can be compared to a bowtie dipole antenna. It can be fed in a similar fashion as shown in Figure 7.1.

This fractal antenna has also been closely studied at the Polytechnic University of Catalonia, Barcelona, Spain by Carles Puente-Baliarda *et al.* [11].

This type of antenna, while not being frequency independent, but having several bands of resonance, can be compared with classical frequency independent antennas such as log-periodics and spirals. These antennas are investigated in detail in [46]. It is known that frequency independence is a result of retaining a similar shape at many scales. It is interesting to point out that while this

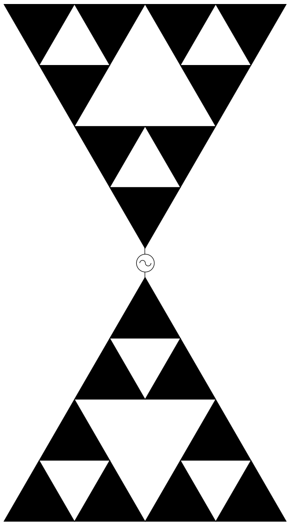

Figure 7.1: Sierpinski sieve fractal fed as a dipole.

property for spirals and log-periodics holds as these antennas grow larger, the self-similarity of the fractal is contained in itself and does not require additional area.

7.1 Fractal Generator and Geometry

The Sierpinski sieve is a good example of a self-similar antenna that shows multiband behavior. The generation of the fractal is shown in Figure 7.2. A Sierpinski sieve dipole can be easily compared to a bowtie dipole antenna, which is the generator to create the fractal. The middle third triangle is removed from the bowtie antenna, leaving three equally sized triangles, which are half the height of the original bowtie. The process of removing the middle third is then repeated on each of the new triangles. For an ideal fractal, this process goes on for an infinite number of times.

Since an infinite number of iterations is impossible to achieve, a finite number can be used to show the multiband characteristics of the antenna. The shapes

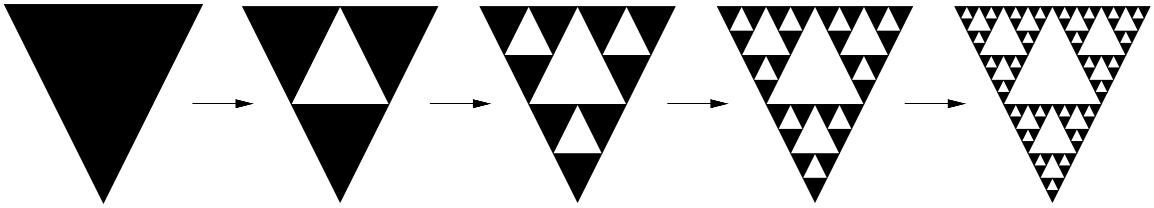

Figure 7.2: Generation of a Sierpinski sieve, starting with a bowtie antenna.

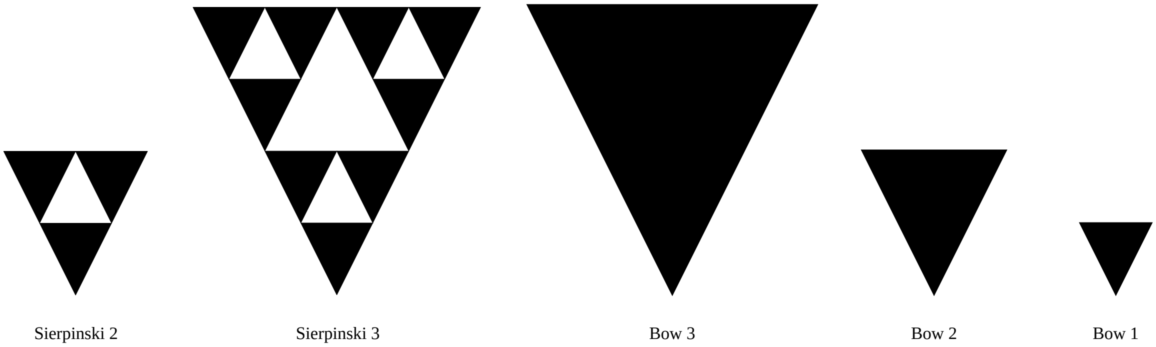

Figure 7.3: Relative sizes of antennas used for multiband comparison.

that are analyzed here are shown in Figure 7.3. A Sierpinski dipole antenna is compared to bowtie dipoles which are scaled versions of the effective antennas contained inside the geometry of the Sierpinski antenna.

7.2 Antenna Analysis

The antennas are fed as dipole antennas, as depicted in Figure 7.1. How the antenna is fed is identical to how a bowtie dipole antenna would be fed. There is a very short segment of wire that connects the two half of the dipoles. The generator is placed in the center of this small segment.

The fractal surface was subsectioned into triangular facets. The geometry of the facets are shown in Figure 7.4 for half of the dipole antenna. The feeding wire is shown in red in the bottom of the figure. The frill voltage source, used to

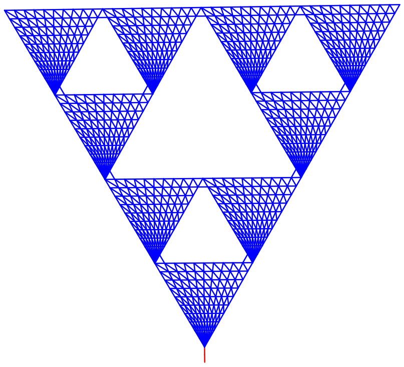

Figure 7.4: Triangular facets and feed wire for Sierpinski antenna simulations.

excite the feeding wire, is connected to the bottom end of this wire in the figure. Also, a small connecting triangle was added to the structure to allow currents to flow from one solid triangle of the sieve to the next. This connecting triangle rounded out the holes cut in the fractal.

The height of the largest antennas, the Sierpinski 3 and Bow 3 antennas, are 22 mm. This height is chosen such that the first and second resonances of these antennas would lie in commonly used bands. The first resonance occurs in C band near 5 GHz and the second resonance occurs in X band near 11 GHz. The height of the other antennas are 11 mm for the Sierpinski 2 and Bow 2 antennas. The Bow 1 antenna is 5.5 mm high. The smaller geometries are the repeated self-similar scales that comprise the Sierpinski 3 antenna. They are tested for comparison purposes. The smaller antennas are expected to operate with equal performance as the scaled effective antennas of the full fractal.

The feeding wire is 1 mm in length and is subsectioned into 3 pieces. At the first resonance of 5 GHz, this length is equal to 0.017 λ. The diameter of this

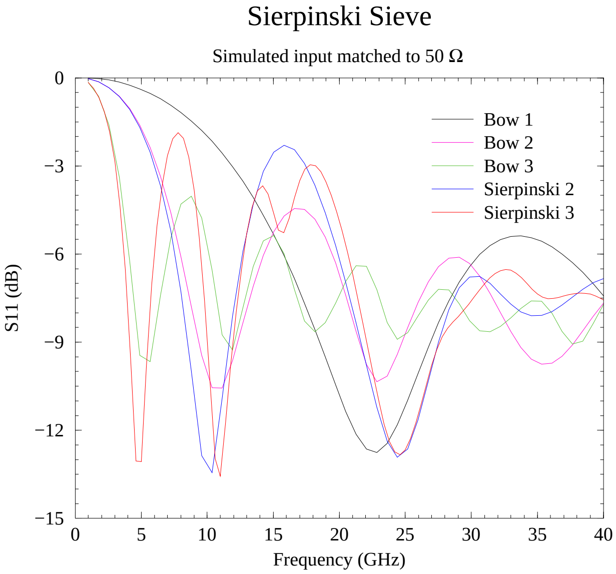

Figure 7.5: Simulated input match of antennas matched to 50 Ω.

subsection is 0.0017 λ at this frequency.

7.3 Antenna Characteristics

The antennas were analyzed using the moment method. From this, the input match of the antennas are attained as shown in Figure 7.5. Three distinct resonances can be seen in the plot of S11.

These three resonances relate to the three sizes of the bowtie antennas and the three self-similar sizes inside the Sierpinski antennas. The physical sizes of these related structures are identical. A true interpretation can be obtained by comparing the resonances of the Sierpinski 3 antenna with the three bowtie antennas that have the same shape as the three scales found in the Sierpinski 3 shape. The Sierpinski 3 antenna matches at three resonances. The largest bowtie antenna, bow 3, matches at the same frequency as the matches of Sierpinski 3. The outline area that these two antennas occupy are the same, and thus their

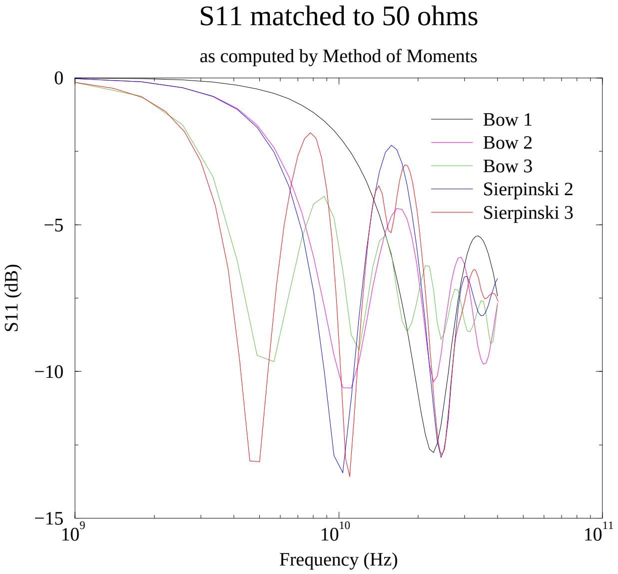

Figure 7.6: Input match of antennas matched to 50 Ω plotted on a logarithmic scale.

lowest resonances are the same, as well. The smallest bowtie antenna, which is the same size as the third self similar iteration of the Sierpinski antenna matches at the third resonance of the Sierpinski antenna.

The highest frequency resonance for the Sierpinski 3 antenna is also the fourth resonance of the largest bowtie antenna, bow 3. This exemplifies the logarithmic nature of the antenna. Plotted in Figure 7.6 is the input match versus frequency on a logarithmic scale. The even logarithmic spacing between the resonances can be seen in this plot. Each resonance is approximately twice that of the one before. This is what would be intuitively expected knowing that the self-similar features of the geometry are scaled by a factor of two for each generating iteration.

The bandwidth of each of the bands is noticeably smaller than that of a bowtie antenna. While the Sierpinski antenna can physically be compared to the bowtie antenna, the bandwidth is only 18% at the highest band. The bandwidth of the bowtie antenna is over 30%.

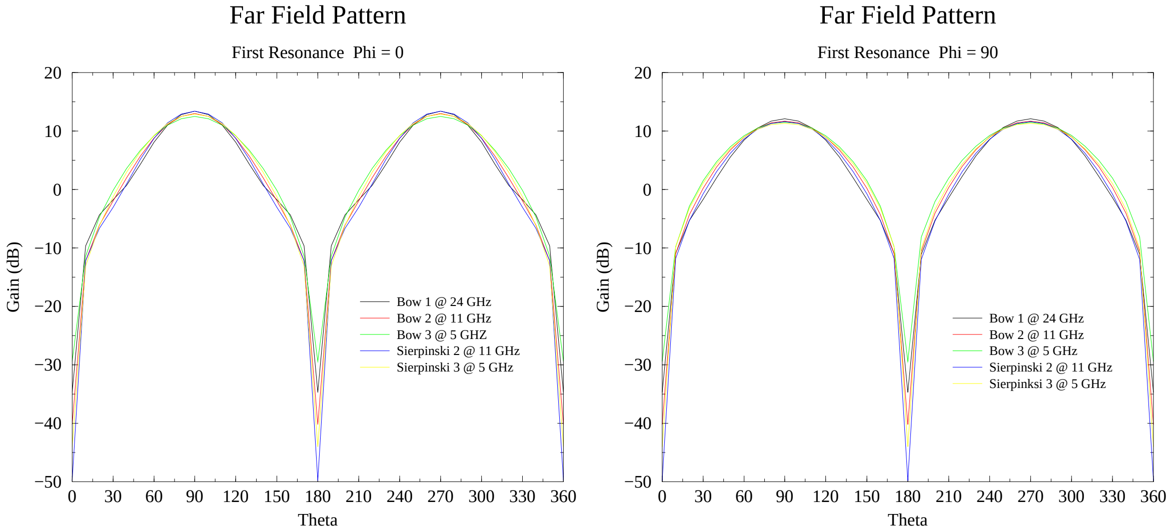

(a) (b)

Figure 7.7: Simulated far field pattern of antennas at first resonance. a) $\phi = 0^o$ cut b) $\phi = 90^o$ cut.

The benefits of the multiband behavior, however, can be seen in the far field pattern plots for these antennas. The far field patterns for the antennas at their first, second, and third resonances are shown in Figure 7.7, Figure 7.8, and Figure 7.9.

The far field patterns at the first two resonances are very similar for each of the antennas in each primary cut. The pattern of the Sierpinski 3 antenna in the $\phi = 0^o$ and $\phi = 90^o$ cuts at the first resonance correspond with the patterns in equivalent cuts calculated at the second resonance. The property of having similar patterns at various resonances is an important parameter for antenna designed for multiband applications.

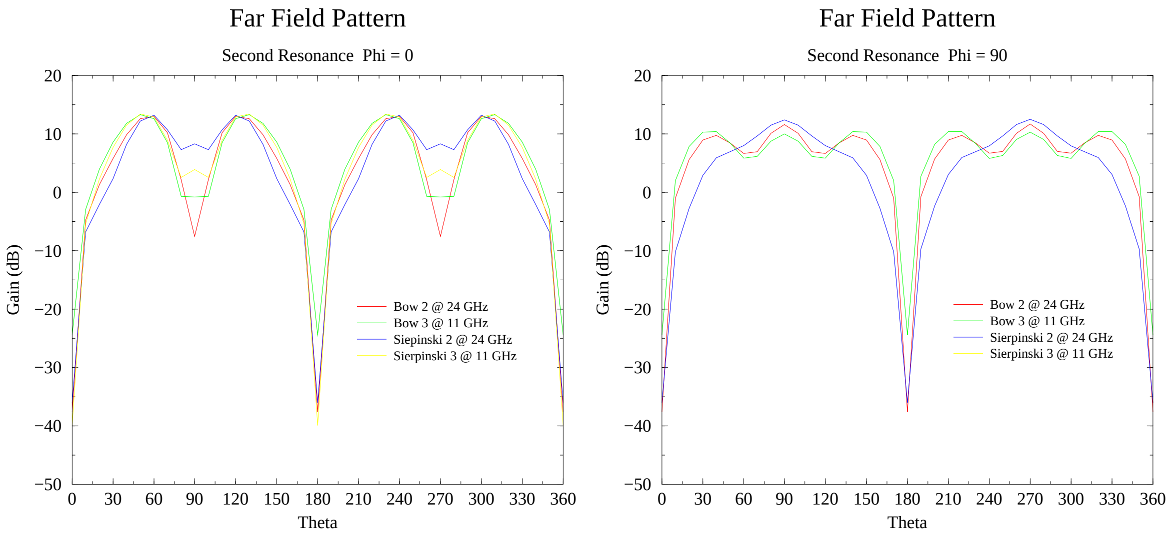

(a) (b)

Figure 7.8: Simulated far field pattern of antennas at second resonance. a) $\phi = 0^o$ cut b) $\phi = 90^o$ cut.

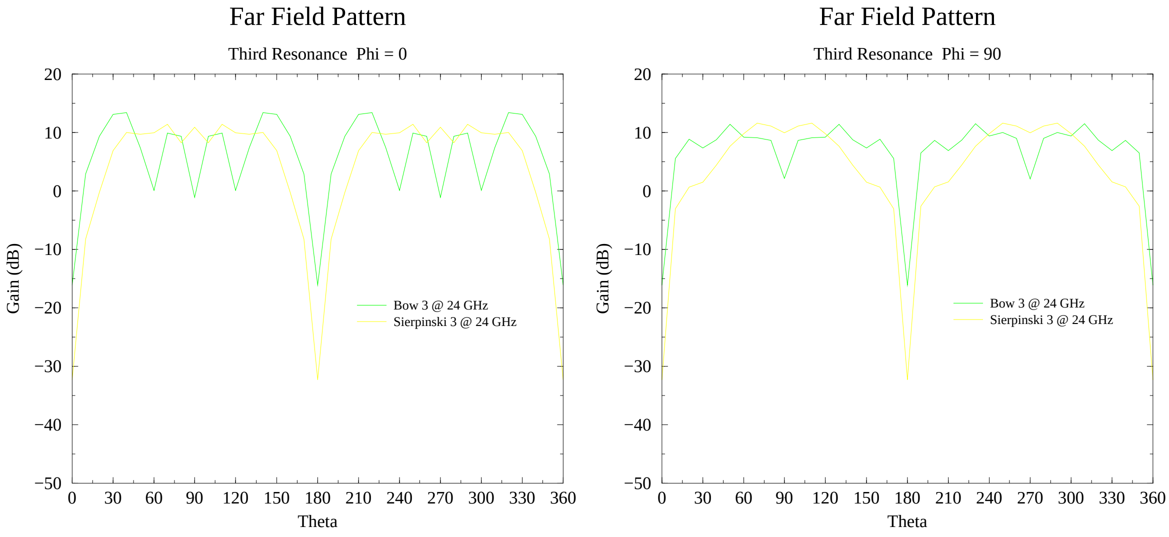

(a) (b)

Figure 7.9: Simulated far field pattern of antennas at third resonance. a) $\phi = 0^o$ cut b) $\phi = 90^o$ cut.

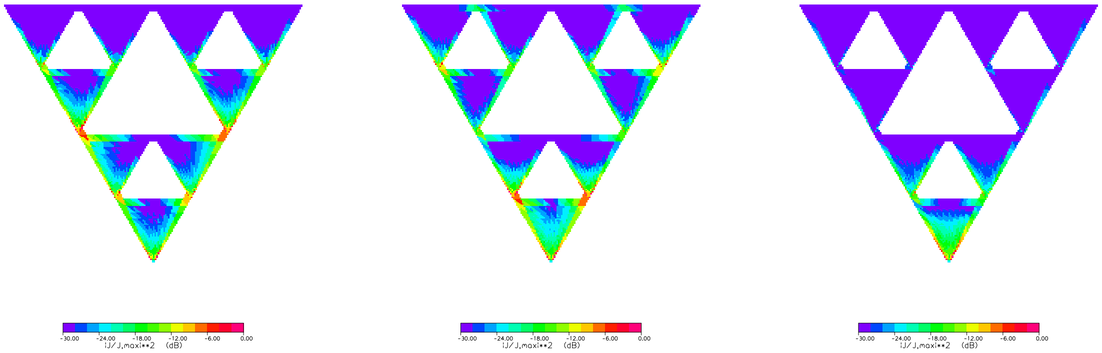

(a) (b) (c)

Figure 7.10: Currents on Sierpinski 3 dipole at a) first resonance, 5 GHz, b) second resonance, 11 GHz, c) third resonance, 24 GHz

7.4 Surface Currents

To understand what part of the antenna is being utilized at each resonance, the calculated surface currents are plotted. The surface currents for the Sierpinski 3 antenna and the bowtie 3 antenna are shown in Figure 7.10 and Figure 7.11.

The current distribution for the bowtie antenna and the Sierpinski antennas gives an intuitive insight into how the antenna is operating at multiple frequencies. The distribution of the current correlates with the self-similar geometry. The surface currents are scaling themselves in the same manner as the geometry. As would be expected, the antenna's excitation is limited to the scaled geometry that would resonate on its own had it been analyzed outside of the fractal. The current distribution of the Sierpinski antenna shows that at the first resonance of 5 GHz, the current is distributed over the entire fractal. However, at the third resonance, 24 GHz, the current is limited to the bottom row triangle of

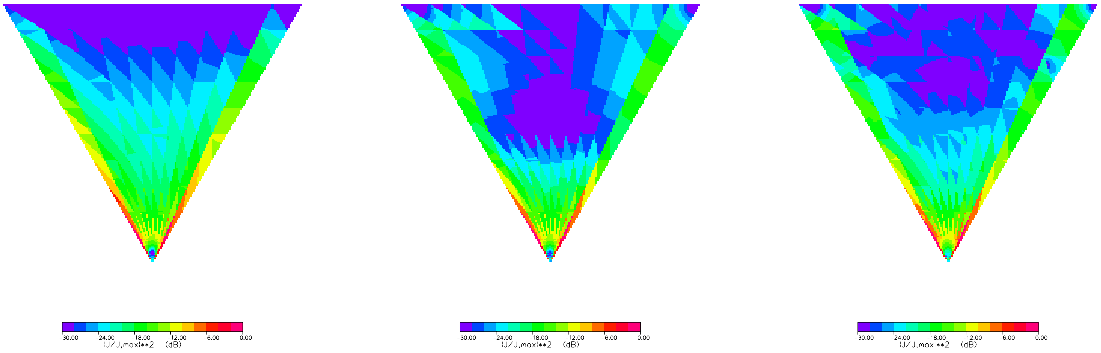

(a) (b) (c)

Figure 7.11: Currents on bow 3 dipole at a) first resonance, 5 GHz, b) second resonance, 11 GHz, c) third resonance, 24 GHz

the fractal. The current distribution of the bowtie antenna at the first resonance resembles those of the three resonances of the Sierpinski antenna. The currents on the bowtie antenna at the second and third resonances are more varied since the antenna is not matched at these frequencies.

CHAPTER 8

Applications of Fractal Antennas

There are many applications that can benefit from fractal antennas. Discussed below are several ideas where fractal antennas can make an real impact.

The sudden growth in the wireless communication area has sprung a need for compact integrated antennas. The space saving abilities of fractals to efficiently fill a limited amount of space create a distinct advantage of using integrated fractal antennas over Euclidean geometries. Examples of these types of applications include personal hand-held wireless devices such as cell phones and other wireless mobile devices such as laptops on wireless LANs and networkable PDAs.

Fractal antennas can also enrich applications that include multiband transmissions. This area has many possibilities ranging from dual-mode phones to devices integrating communication and location services such as GPS, the global positioning satellites.

Fractal antennas also decrease the area of a resonant antenna, which could lower the radar cross-section (RCS). This benefit can be exploited in military applications where the RCS of the antenna is a very crucial parameter.

Phased array antennas are another example of an application that can take advantage of the miniaturization of loop and dipole elements. This idea is developed further in the next section.

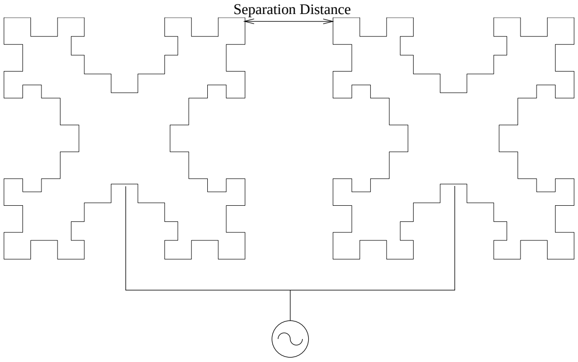

Figure 8.1: Array of two fractal square loops. Separation distance is the shown as the distance between the edges of the elements.

8.1 Fractal Elements in Array Antennas

An enhancement to a phased array is a very wide scan angle, which requires the elements to be very close together. Besides the obvious limitation of the width of the elements, mutual coupling between the elements also limits the minimum spacing, which decreases the scan angle.

Fractal loop elements are smaller than Euclidean resonant loops and can, thus, have closer inter-element spacings while maintaining the edge-to-edge separations. Mutual coupling changes the excitation current of each element causing distortions in the radiation patterns. An array of two loop elements depicting the edge-to-edge separation distance is shown in Figure 8.1.

8.1.1 Reduced Mutual Coupling

The design of phased array antennas needs to take into account mutual coupling. The effects of mutual coupling usually include the filling in of nulls and the raising of the level of back radiation [45].

One attempt to control mutual coupling between the elements of an array

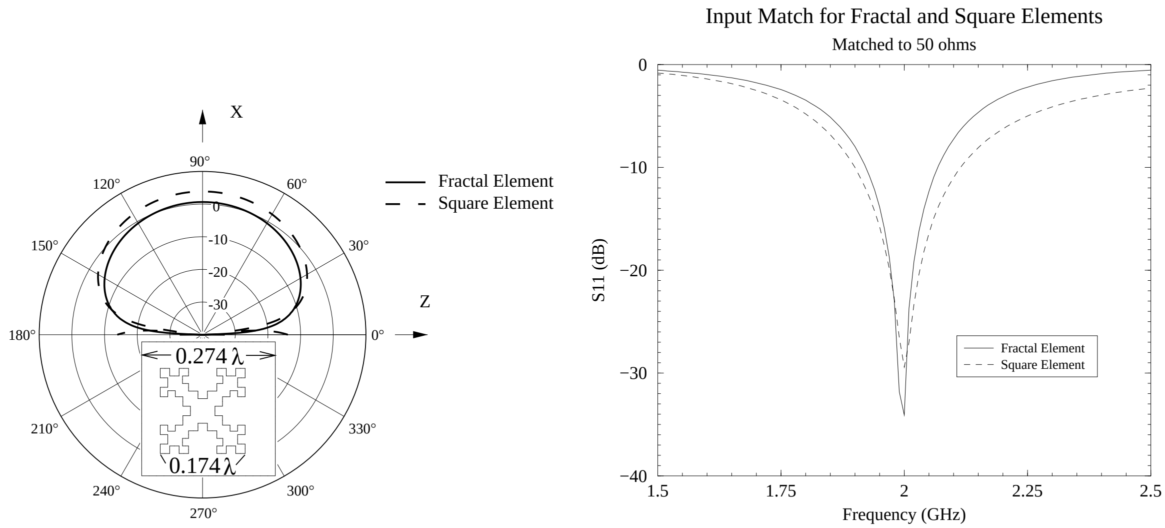

(a) (b)

Figure 8.2: a) Far field patterns and b) S11 input impedance matched to 50 Ω for the loop elements used in the arrays of this chapter. The relative sizes of the two loops is drawn inset in (a).

is to increase the edge-to-edge spacing. For an array designed for a particular pattern, the spacing between the edges of the elements is dictated by the desired pattern and the width of the element. Hence, miniaturized elements can be used to increase this spacing.

To verify the above observations, an array has been designed comparing standard square loop elements to fractal loop elements. The fractal that is employed for this application is a third order Minkowski square loop, studied in section 5.2. The two loop elements are designed to be resonant at the same frequency. Their input impedance and far field patterns are shown in Figure 8.2. The arrays are simulated as wire loop elements in free space.

The test case for comparing the two arrays is a 5 element, Dolph-Chebyshev linear array scanned to 150^o off of the axis of the array. The array is designed

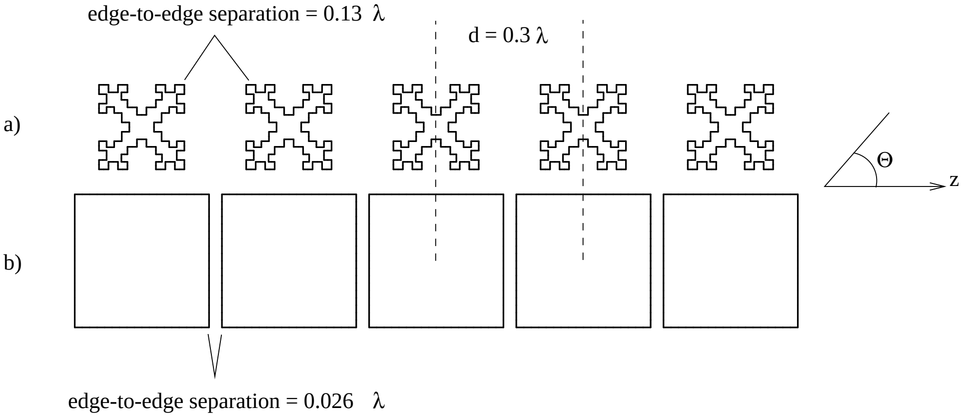

Figure 8.3: Relative geometry for the two arrays using a) Minkowski square loop elements, and b) using standard square loop elements. The space between the elements is increased for the array with fractal elements.

for -30 dB sidelobes with 0.3λ spacing. The voltage excitation for this type of array have the ratios of $1{:}2.41e^{-j1.632}{:}3.41e^{-j3.264}{:}2.41e^{-j4.896}{:}1e^{-j6.528}$, as given in [45]. These excitation coefficients have a high volatility between the elements providing a setting with a strong potential for adverse mutual coupling. The relative geometry of the two arrays is summarized in Table 8.1 and is shown in Figure 8.3.

Table 8.1: Specifications used in the design of arrays showing reduced mutual coupling with fractal elements.

	Spacing	Edge-to-Edge	Progressive Phase (rad)
Square Loop	0.3λ	0.026λ	1.632
Minkowski Fractal Loop	0.3λ	0.13λ	1.632

The simulated far field patterns are plotted in Figure 8.4. The plots are the normalized directivity for the two arrays, plus the normalized directivity of an

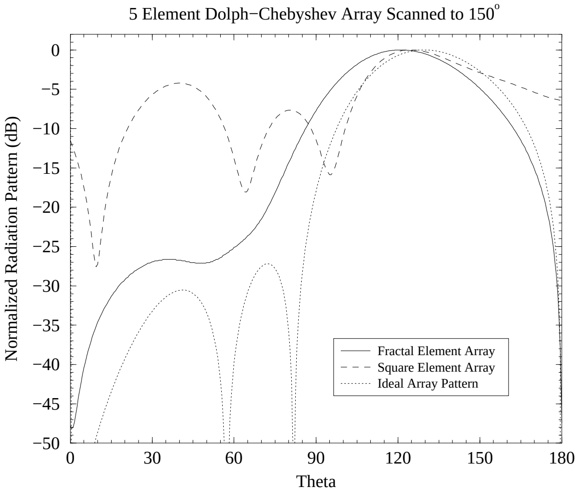

Figure 8.4: Normalized, simulated directivity patterns for 5 element, Dolph-Chebyshev, 0.3λ spaced linear array scanned to 150^o. The three plots shown include the simulated patterns using fractal square elements, square elements, and the ideal pattern as expected without mutual coupling.

ideal array without mutual coupling. The ideal pattern is generated using the known linear array equation with a $\sin(\theta)$ element pattern [45]. The formula for the complete pattern is given in Eq. (8.1.1).

$$f(\theta) = \sin(\theta) \sum_{n=0}^{N-1} A_n e^{jn\psi} \tag{8.1.1}$$

where $\psi = \beta d \cos\theta + \alpha$, $\beta = 2\pi/\lambda$, λ is the wavelength, d is the center-to-center spacing between the elements, α is the progressive phase of the excitation of the elements, and A_n are the excitation coefficients.

It can be seen from the normalized directivity patterns of Figure 8.4 how mutual coupling adversely affects the arrays. Mutual coupling effects both of the arrays, with square elements and with fractal elements, however, the results are closer to what was expected with the fractal elements. While the ideal pattern

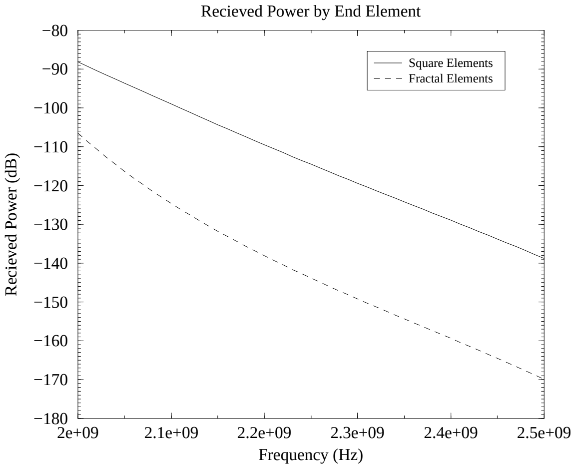

Figure 8.5: Simulated received power by the end element of the array with the other 4 elements radiating normally.

predicts a back radiation, $\theta = 30^o$, of -30 dB, from the design, the back radiation of the array with fractal elements is -26.8 dB down and the back radiation from the square element array is -4.3 dB.

The received power of the end element shows how the mutual coupling is decreased for the fractal element array. The simulated received power of the end element with the other 4 elements radiating normally is plotted in Figure 8.5.

8.1.2 Tighter Array Packing

Another method of implementing the smaller dimensions of resonant fractal antennas is to pack more elements into a linear array. The smaller elements would allow for denser packed arrays. The following example is a densely packed array using fractal elements. In the space of a five element array of square loop elements space 0.5λ apart, seven resonant fractal loop elements would fit, spaced 0.35λ apart, maintaining the edge-to-edge separation between the elements for both the square and fractal arrays. This decrease in spacing between the centers of the elements results in arrays that can be scanned closer to the axis of the array.

The elements that are used for this example are the same elements that are used in the previous section, whose performances are shown in Figure 8.2. The spacing and geometry of both arrays are shown in Figure 8.6. The overall length of the array is maintained, as well as the edge-to-edge separation between the elements. The spacing of the square element array is 0.5λ, while the fractal element array has a center-to-center spacing of 0.35λ. Both arrays are uniformly excited with a progressive phase to scan the main beam to 150^o from the axis of the array, as seen in Table 8.2.

Table 8.2: Specifications used in the design of arrays showing denser packing with fractal elements.

	Spacing	Edge-to-Edge	Progressive Phase (rad)
Square Loop	0.5λ	0.23λ	2.72
Minkowski Fractal Loop	0.35λ	0.18λ	1.9

The simulated far field patterns of the two arrays are compared in Figure 8.7. Also plotted is the ideal patterns for the appropriate spacing and phasing computed from Eq. (8.1.1). It can be seen how mutual coupling raises the back radiation, $\theta = 30^o$, of both the square element and the fractal element array by about the same amount. However, from the design, the back radiation of the fractal element array is 15 dB below that of the square element array.

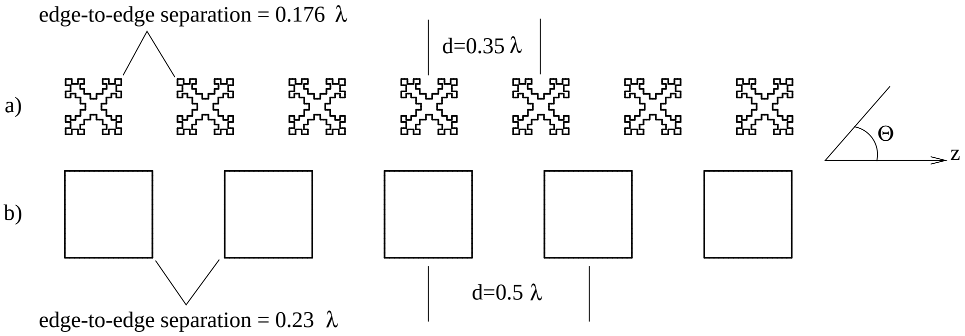

Figure 8.6: Relative geometry for the two arrays using a) Minkowski square loop elements, and b) using standard square loop elements. The total width of the array is maintained for the two arrays. The edge-to-edge separation between the elements is similar for the two arrays.

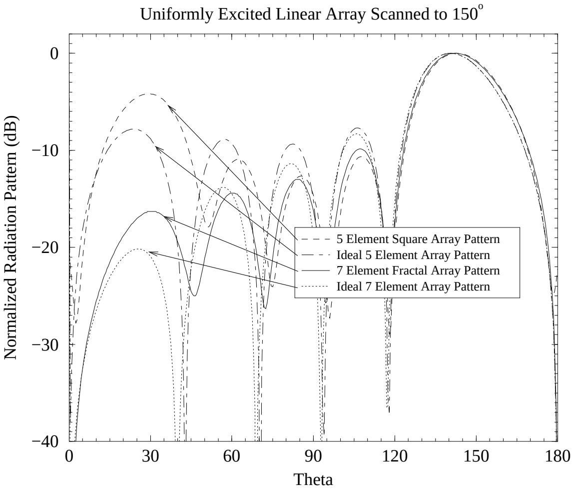

Figure 8.7: Simulated directivity patterns for a 5 element, 0.5λ spaced array of square elements and a 7 element, 0.35λ spaced array of fractal elements, both scanned to 150^o, uniformly excited, and having equal total lengths. Also plotted are the ideal patterns of the 5 and 7 element arrays with uniform excitation neglecting mutual coupling.

CHAPTER 9

Conclusion

Fractal geometry was first brought to light by Benoit Mandelbrot in 1975 as a way to mathematically define structures whose dimension can not be limited to whole numbers. These geometries have been used previously to characterize unique occurrences in nature that were difficult to define with Euclidean geometries. These examples in nature include the length of coastlines, the density of clouds, and the branching of trees.

Just as nature is not confined to Euclidean geometries, antenna designs should not be confined, as well. Looking at geometries whose dimensions are not limited to integers may lead to the discovery of antennas with improved characteristics over that which exist today. Presented in this thesis is a collection of several fractal geometries implemented as antennas that can serve as an overview to the infinite possibilities opened up by fractals. The fractals have shown the possibility to miniaturize antennas and to improve input matching. Certain classes of fractal geometries operate effectively as antennas at various frequency bands.

The miniaturization of the antennas has been explored for wire loop and dipole antennas. There exists a variety of fractal geometries that can be implemented as antennas. Several examples have been simulated and fabricated in this work. Two different island fractals have been implemented into loop configurations observing two different benefits, improved input match and reduced size. Three different fractal configurations were tested as dipoles with the intent of miniaturizing the antennas.

The first advantage in using a fractal loop is how the fractal miniaturizes a resonant loop antenna. By using a Minkowski fractal as a resonant square loop, 36% of the total width can be saved over using a resonant square loop. Also, the input match and far field patterns of the two antennas are very similar. The second advantage occurs when using a fractal loop antenna below resonance, where a typical small loop would have a very low input impedance, which is difficult to match. Using a Koch island fractal as a small loop, increased the input impedance to 35 Ω from 1 Ω for an equal radius circular loop.

The three fractals that were studied as dipole antennas included a Koch fractal, a fractal tree, and a three dimensional version of the fractal tree. The intent of investigating these antennas was to find an effective method of miniaturization. The results show that the two dimensional structures miniaturized the antennas to a similar degree. However, the three dimensional dipole decreases the height requirement by an even greater degree.

Also in this work, fractals that are particularly well-suited to multiband operation are studied. The self similar nature of the geometry of a Sierpinski sieve fractal results in very similar antenna characteristics across many bands as defined by the geometry. The current distribution on the antenna gives some insight into why this particular fractal acts so well at various bands.

Furthermore, fractal antennas can be configured to be used in a variety of unique applications that take advantage of their space-saving and improved matching characteristics. One example of this includes phased arrays. Using fractal antennas in the design provides decreased mutual coupling and improved scanning performance. Other applications that can benefit by using fractal antennas are discussed.

In the future, fractal antennas can be studied in several areas. One area of development is to implement fractal antennas into current technologies in practical situations, such as the expanding wireless market. For this application, a rigorous analysis of the polarization of these antennas will need to be investigated. Another benefit that can be explored is the lower encompassed area of resonant loop antennas. This may lead to antennas with lower radar cross sections. Also, fractals can be looked at as microstrip antennas and their excitation of surface waves. Fractals may be able to be configured to further decrease mutual coupling in arrays by decreasing the excitation of surfaces waves when the arrays are printed on a dielectric.

Another area of interest worth pursuing is to analyze the mathematical aspects of fractals to correlate their improved characteristics as antennas with their unique geometrical properties.

References

[1] Roger B.J. Baron. Fractal landscape 280294. http://perso.club-internet.fr/regor/F-Render/index.html, 1994.

[2] Benoit B. Mandelbrot. *The fractal geometry of nature.* W.H. Freeman, 1982.

[3] Richard P. Feynman, Robert B. Leighton, and Matthew Sands. *The Feynman Lectures on Physics: mainly mechanics, radiation, and heat.* Addison-Wesley Publishing Compnay, Menlo Park, California, 1963.

[4] H.N. Kritikos and D.L. Jaggard, editors. *Recent Advances in Electromagnetic Theory*, chapter 6, pages 183–224. Springer-Verlag, 1990.

[5] D.H. Werner and P.L. Werner. Frequency-independent features of self-similar fractal antennas. *Radio Science*, 31(6):1331–43, November-December 1996.

[6] D.H. Werner, P.L. Werner, and A.J. Ferraro. Frequency-independent features of self-similar fractal antennas. In *IEEE Antennas and Propagation Society*, volume 3, pages 2050–3, July 1996.

[7] X. Yang, J. Chiochetti, D. Papadopoulos, and L. Susman. Fractal antenna elements and arrays. *Applied Microwave and Wireless*, 11(5):34,36,38,40,42,44,46, May 1999.

[8] Jacques Levy Vehel, Evelyne Lutton, and Claude Tricot, editors. *Fractals in engineering*, chapter Fractals and Waves. Springer, 1997.

[9] Douglas H. Werner and Raj Mittra, editors. *Frontiers in Electromagnetics.* IEEE Press Series on Microwave Technology and RF. IEEE Press, 2000.

[10] C. Puente, J. Romeu, R. Pous, X. Garcia, and F. Benitez. Fractal multiband antenna based on the sierpinski gasket. *Electronics Letters*, 32(1):1–2, January 1996.

[11] C. Puente-Baliarda, J. Romeu, R. Pous, and A. Cardama. On the behavior of the sierpinski multiband fractal antenna. *IEEE Transactions on Antennas and Propagation*, 46(4):517–524, April 1998.

[12] C. Puente, J. Romeu, R. Bartoleme, and R. Pous. Perturbation of the sierpinski antenna to allocate operating bands. *Electronics Letters*, 32(24):2186–8, November 1996.

[13] C. Puente, M. Navarro, J. Romeu, and R. Pous. Variations on the fractal sierpinski antenna flare angle. In *IEEE Antennas and Propagation Society*, volume 4. IEEE Antennas and Propagation Society, June 1998.

[14] R. Breden and R.J. Langley. Printed fractal antennas. In *IEE National Conference on Antennas and Propagation*, pages 1–4, April 1999.

[15] J.M. Gonzalez, M. Navarro, C. Puente, J. Romeu, and A. Aguasca. Active zone self-similarity of fractal-sierpinski antenna verified using infra-red thermograms. *Electronics Letters*, 35(17):1393–4, August 1999.

[16] C. Borja, C. Puente, and A. Medina. Iterative network model to predict the behaviour of a sierpinski fractal network. *Electronics Letters*, 34(15):1443–5, July 1998.

[17] Liang Xu and M.Y.W. Chia. Multiband characteristics of two fractal antennas. *Microwave and Optical Technology Letters*, 23(4):242–5, November 1999.

[18] Jesus Fornieles Callejon, Amelia Rubio Bretones, and Rafael Gomez Martin. On the application of parametric models to the transient analysis of resonant and multiband antennas. *IEEE Transactions on Antennas and Propagation*, 46(3):312–17, March 1998.

[19] G.J. Walker and J.R. James. Fractal volume antennas. *Electronics Letters*, 34(16):1536–7, August 1998.

[20] C.T.P. Song, P.S. Hall, H. Ghafouri-Shiraz, and D. Wake. Fractal stacked monopole with very wide bandwidth. *Electronics Letters*, 35(12):945–6, June 1999.

[21] J. Romeu and Y. Rahmat-Samii. Dual band fss with fractal elements. *Electronics Letters*, 35(9):702–3, April 1999.

[22] N. Cohen. Fractal antennas part 1: Introduction and the fractal quad. *Communications Quarterly*, pages 7–22, Summer 1995.

[23] N. Cohen. Fractal antennas part 2: A discussion of relevant, but disparate, qualities. *Communications Quarterly*, pages 53–66, Summer 1996.

[24] N. Cohen. Fractal antenna applications in wireless telecommunications. In *Professional Program Proceedings*, pages 43–9. Electronic Industries Forum of New England, May 1997.

[25] C. Puente, J. Romeu, R. Pous, J. Ramis, and A. Hijazo. Small but long koch fractal monopole. *Electronics Letters*, 34(1):9–10, January 1998.

[26] R.G. Hohlfeld and N. Cohen. Self-similarity and the geometric requirements for frequency independence in antennae. *Fractals*, 7(1):79–84, March 1999.

[27] C. Puente, J. Claret, F. Sagues, J. Romeu, M.Q Lopez-Salvans, and R. Pous. Multiband properties of a fractal tree antenna generated by electrochemical deposition. *Electronics Letters*, 32(25):2298–9, December 1996.

[28] M. Sindou, G. Ablart, and C. Sourdois. Multiband and wideband properties of printed fractal branched antennas. *Electronics Letters*, 35(3):181–2, February 1999.

[29] D.H. Werner, A. Rubio Bretones, and Long B.R. Radiation characteristics of thin-wire ternary fractal trees. *Electronics Letters*, 35(8):609–10, April 1999.

[30] C. Puente-Baliarda and R. Pous. Fractal design of multiband and low sidelobe arrays. *IEEE Transactions on Antennas and Propagation*, 44(5):730–9, May 1996.

[31] D.H. Werner and R.L. Haupt. Fractal constructions of linear and planar arrays. In *IEEE Antennas and Propagation Society*, volume 3, July 1997.

[32] Douglas H. Werner, Randy L. Haupt, and Pingjuan L. Werner. Fractal antenna engineering: The theory and design of fractal antenna arrays. *IEEE Antennas and Propagation Magazine*, 41(5):37–59, October 1999.

[33] Dwight L. Jaggard and Aaron D. Jaggard. Cantor ring arrays. *Microwave and Optical Technology Letters*, 19(2):121–5, October 1998.

[34] Dwight L. Jaggard and Aaron D. Jaggard. Cantor ring arrays. In *IEEE Antennas and Propagation Society*, volume 2, pages 862–5, 1998.

[35] Xu Liang, Wu Zhensen, and Wang Wenbing. Synthesis of fractal patterns from concentric-ring arrays. *Electronics Letters*, 32(21):1940–1, October 1996.

[36] Liang Xu, Zhen-Sen Wu, and Wen-Bing Wang. Fractal linear arrays. *Chinese Physics Letters*, 15(2):140–2, 1998.

[37] T. Aubreton, P. Vaudon, and B. Jecko. Theoretical analysis of a fractal surface radiation. *Annales des Telecomminications*, 52(7-8):427–34, July-Aug 1997.

[38] D.H. Werner, K.C. Anushko, and P.L. Werner. The generation of sum and difference patterns using fractal subarrays. *Microwave and Optical Technology Letters*, 22(1):54–7, July 1999.

[39] Benoit B. Mandelbrot. *Fractals: Form, chance, and dimension.* W.H. Freeman and Company, 1977.

[40] R.E. Hodges and Y. Rahmat-Samii. An iterative current-based method for complex structures. *IEEE Transactions on Antennas and Propagation*, 45(2):265–276, February 1997.

[41] R.E. Hodges and Y. Rahmat-Samii. Physical optics hybrid method: Analytical details. Technical report, University of California, Los Angeles, Dept. of Electrical Engineering, University of California, School of Engineering and applied science, Los Angeles, CA 90024-1594, 1993.

[42] John Gianvittorio. Farfield measurement capabilities at ucla's antenna lab. http://www.antlab.ee.ucla.edu/j̃ohng/farfield.html, May 2000.

[43] CHFE webmaster. Chfe - circuit etching. www.chfe.ee.ucla.edu, January 2000.

[44] C. A. Balanis. *Antenna Theory: Analysis and Design.* John Wiley and Sons, New York, 1997.

[45] W. L. Stutzman and G. A. Thiele. *Antenna Theory and Design.* John Wiley and Sons, second edition, 1998.

[46] R.S. Elliott. *Antenna theory and design.* Prentice-Hall, New Jersey, 1981.